



Stellar inventory of the solar neighbourhood using *Gaia* DR1

Jo Bovy^{1,2★†}

¹Department of Astronomy and Astrophysics, University of Toronto, 50 St. George Street, Toronto, ON M5S 3H4, Canada

²Center for Computational Astrophysics, Flatiron Institute, 162 5th Ave, New York, NY 10010, USA

Accepted 2017 May 19. Received 2017 May 18; in original form 2017 April 12

ABSTRACT

The absolute number and the density profiles of different types of stars in the solar neighbourhood are a fundamental anchor for studies of the initial mass function, stellar evolution, and Galactic structure. Using data from *Gaia* DR1, we reconstruct *Gaia*'s selection function and determine *Gaia*'s volume completeness, the local number density, and the vertical profiles of different spectral types along the main sequence from early A stars to late K stars as well as along the giant branch. We clearly detect the expected flattening of the stellar density profile near the mid-plane: All vertical profiles are well represented by sech^2 profiles, with scaleheights ranging from ≈ 50 pc for A stars to ≈ 150 pc for G and K dwarfs and giants. We determine the luminosity function along the main sequence for $M_V < 7$ ($M \gtrsim 0.72 M_\odot$) and along the giant branch for $M_J \gtrsim -2.5$ in detail. Converting this to a mass function, we find that the high-mass ($M > 1 M_\odot$) present-day mass function along the main sequence is $dn/dM = 0.016(M/M_\odot)^{-4.7}$ stars $\text{pc}^{-3} M_\odot^{-1}$. Extrapolating below $M = 0.72 M_\odot$, we find a total mid-plane stellar density of $0.040 \pm 0.002 M_\odot \text{ pc}^{-3}$. Giants contribute 0.00039 ± 0.00001 stars pc^{-3} or about $0.00046 \pm 0.00005 M_\odot \text{ pc}^{-3}$. The star formation rate surface density is $\Sigma(t) = 7 \pm 1 \exp(-t/7 \pm 1 \text{ Gyr}) M_\odot \text{ pc}^{-2} \text{ Gyr}^{-1}$. Overall, we find that *Gaia* DR1's selection biases are manageable and allow a detailed new inventory of the solar neighbourhood to be made that agrees with and extends previous studies. This bodes well for mapping the Milky Way with the full *Gaia* data set.

Key words: stars: statistics – Galaxy: disc – Galaxy: fundamental parameters – solar neighbourhood – Galaxy: stellar content – Galaxy: structure.

1 INTRODUCTION

The Milky Way is a cornerstone in our understanding of the structure and evolution of galaxies. And within the Milky Way, the solar neighbourhood provides a fundamental basis for studies of Galactic structure, star formation and stellar evolution, and Galactic dynamics. Within a few hundred parsecs from the Sun, we can see stars that span the extremes from the most luminous main-sequence and giant stars to the faintest M dwarfs. This provides an essential basis for understanding the baryonic content of the Milky Way and external galaxies as it allows the initial mass function (IMF; e.g. Gould, Bahcall & Flynn 1996; Kroupa 2001; Chabrier 2001), the mass-to-light ratio (e.g. Flynn et al. 2006), and the local star formation history (e.g. Binney, Dehnen & Bertelli 2000) to be determined directly. A complete baryonic census of the solar neighbourhood is also important for comparing with dynamical determinations of the local mass distribution, which are only sensitive to the combined

mass in baryons and dark matter (e.g. Holmberg & Flynn 2000; Bovy & Rix 2013).

The most precise censuses of stars in the solar neighbourhood are largely based on small, volume-complete surveys of local stars (for example within 25 pc, Reid, Gizis & Hawley 2002; within 50 pc, Jahreiss, Wielen & Fuchs 1998), which contain only a handful of the most luminous stars. While this does not matter for determining the IMF from the number density of long-lived stars, for the purpose of, e.g. measuring the local stellar density distribution and comparing it to dynamical estimates (McKee, Parravano & Hollenbach 2015), small volumes centred on the Sun are potentially biased, because the Sun is likely offset from the mid-plane of the Galaxy by 15–25 pc (e.g. Binney, Gerhard & Spergel 1997; Chen et al. 2001; Jurić et al. 2008). Extending the local stellar census to a few hundred parsecs would allow a much better determination of the bright end of the stellar luminosity function and of the present-day mass function.

The European Space Agency (ESA) *Gaia* mission has been designed to investigate the luminous and dark matter distribution within the Milky Way to constrain its formation and evolution (Gaia Collaboration et al. 2016a). While *Gaia* will observe more than 1 billion stars, these constitute only about 1 per cent of all of the stars

* E-mail: bovy@astro.utoronto.ca

† Alfred P. Sloan Fellow.

in the Milky Way and the volume completeness for different types of stars will be complex even in the final data release (DR) due to variations in stellar colours, interstellar extinction, stellar density, and the observation pattern in different parts of the sky. *Gaia* released its first data in the Fall of 2016 (Gaia Collaboration et al. 2016b), which consists of the primary *Tycho-Gaia Astrometric Solution* (*TGAS*) containing positions, parallaxes, and proper motions for a subset of the *Tycho-2* catalog (Høg et al. 2000) and the secondary data set with approximate positions for stars brighter than $G \approx 20.7$ in the wide *Gaia* photometric bandpass G (Lindegren et al. 2016). Based on 14 months of data and a preliminary astrometric processing, the *Gaia* DR1 *TGAS* catalog contains 2 057 050 stars with parallaxes with typical uncertainties of ≈ 0.3 mas. As such, *TGAS* is by far the largest catalogue of trigonometric, high-precision parallaxes for a uniformly selected sample of stars. However, no estimate of the completeness of *TGAS* is provided in the data products. This makes it difficult to use the *TGAS* data to investigate the spatial and dynamical structure of the solar neighbourhood and many of the first uses of the *TGAS* data have therefore focused on purely kinematic studies that do not require knowledge of the selection function (e.g. Allende Prieto, Kawata & Cropper 2016; Hunt, Bovy & Carlberg 2016; Bovy 2017; Helmi et al. 2017).

This paper has two main parts. The first part consists of an extensive discussion of the volume completeness of the *TGAS* catalog for different stellar types. This may be useful to other studies employing *TGAS* data to study various aspects of the Milky Way's structure. It can also be straightforwardly extended to the *Gaia* DR2 data when they appear. The second part uses the volume completeness combined with star counts for different classes of stars to perform a new stellar census of the solar neighbourhood, covering main-sequence stars from early A-type to late K-type dwarfs and giant stars from the subgiant branch to the upper red giant branch (RGB). We also determine the vertical density profiles for these stellar types up to a maximum of 400 pc above the Galactic mid-plane. The resulting census is consistent with previous work and constitutes the most precise determination of the mass distribution in the solar neighbourhood within the mass range observed in *TGAS*.

The structure of this paper is as follows. We introduce our approach to determining stellar densities and their spatial dependence from incomplete surveys in Section 2. In particular, we introduce the effective volume completeness, which for a given small volume in the Galaxy and a given stellar type represents the fraction of stars observed by the survey. In Section 3, we apply this formalism to the *Gaia* DR1 catalog and determine the completeness of the *TGAS* catalog for different stellar types: spectral types along the main sequence and giants in various luminosity ranges. The results from Section 3 depend on a detailed understanding of the ‘raw’ *TGAS* selection function: the fraction of true stars contained in the catalogue as a function of sky position, colour, apparent magnitude, etc. We determine this raw selection function directly from the *TGAS* catalog by comparing it to the Two Micron All Sky Survey (2MASS) catalog (Skrutskie et al. 2006); this is discussed in detail in Appendix A.

In Section 4, we apply the formalism from Section 2 to measure the mid-plane densities and the vertical density profile of different stellar types along the main sequence and fit parametric density laws. From this, we determine the luminosity function, present-day mass function, total mid-plane number and mass densities, and the star formation history of the solar neighbourhood. In Section 5, we similarly measure the mid-plane densities and the vertical density profile for different types of giant stars and determine the luminosity function along the giant branch and the total mid-plane number and

mass density of giants. One of the parameters that we fit for each stellar type is the Sun's offset from the mid-plane as defined by that stellar type and we discuss the resulting offsets in detail in Section 6. We discuss some additional aspects of our results in Section 7 and conclude in Section 8. The basic data that we use throughout this paper come from the *TGAS* catalog (Gaia Collaboration et al. 2016b) matched to photometry from the 2MASS catalog using a 4'' nearest-neighbour search. Various cuts on this basic data set for different applications are described in the text below. We express the volume completeness in rectangular Galactic coordinates (X, Y, Z) , centred on the Sun with X towards the Galactic centre, Y in the direction of Galactic rotation, and Z directed towards the North Galactic Pole. We do not make any use of Galactocentric coordinates or any sort of kinematics and our results therefore do not depend on any assumed value of the standard Galactic constants (e.g. the distance to the Galactic centre or the Sun's velocity).

2 STELLAR NUMBER DENSITY LAWS FROM INCOMPLETE SURVEYS

Our goal is to determine the intrinsic stellar number density distribution $\nu_*(X, Y, Z)$, where (X, Y, Z) is a set of heliocentric Cartesian coordinates, of different stellar populations from *TGAS* observations of their three-dimensional position (α, δ, D) [right ascension, declination, and distance]. If *TGAS* observed all stars in the Galaxy, we would simply count the stars in small volumes and divide this number by the volume to get the density in terms of stars pc⁻³. However, because *TGAS* only observes stars in a finite magnitude range and because even at peak completeness it does not contain all stars, the situation is not quite this simple.

The problem of determining stellar number density laws $\nu_*(X, Y, Z)$ of stellar populations in the Milky Way has a long history (e.g. Bok 1937; Bahcall 1986; Jurić et al. 2008) and has been discussed recently by Bovy et al. (2012b, 2016). The discussion there focused primarily on spectroscopic surveys and on the problem of fitting a parametric density law to star count data. The focus here is different, in that we aim to determine the density $\nu_*(X, Y, Z)$ non-parametrically in bins in (X, Y, Z) from data that cover a substantial fraction of the sky. Much of the discussion, especially about the effect of dust extinction, in this section follows that in Bovy et al. (2016).

We discuss how we determine the *TGAS* completeness as a function of $(J, J - K_s, \alpha, \delta)$ by comparing the number counts in *TGAS* to those in 2MASS in Appendix A. Thus, we have a function $S(J, J - K_s, \alpha, \delta)$ that gives the fraction of stars at a given $(J, J - K_s, \alpha, \delta)$ contained in the *TGAS* catalog. As discussed in Appendix A, we only determine the completeness in the 48 per cent of the sky with ‘good’ *TGAS* observations and within this region, the completeness is independent of (α, δ) ; therefore essentially $S(J, J - K_s, \alpha, \delta) = S(J, J - K_s) \Theta([\alpha, \delta]$ in ‘good’ part of the sky), where $\Theta(a)$ is the function that is one when a holds true and zero otherwise. However, for generality, we will write all expressions in terms of the full $S(J, J - K_s, \alpha, \delta)$.

2.1 Generalities

We determine $\nu_*(X, Y, Z)$ from a data set of stars that is not complete in any (simple) geometric sense and thus we need to take the selection function $S(J, J - K_s, \alpha, \delta)$ into account. The connection between the selection function $S(J, J - K_s, \alpha, \delta)$ and the three-dimensional position (X, Y, Z) is made through a colour-magnitude

density (CMD) $\rho_{\text{CMD}}(M_J, [J - K_s]_0 | X, Y, Z)$ that gives the distribution in (absolute magnitude and unreddened colour), potentially a function of position, that allows us to relate the observed $(J, J - K_s, \alpha, \delta)$ to (X, Y, Z) through the distance and three-dimensional extinction map. While these could (and should) in principle be inferred simultaneously with the stellar density, we assume in what follows that the CMD $\rho_{\text{CMD}}(M_J, [J - K_s]_0 | X, Y, Z)$ and the three-dimensional extinction map $(A_J, E(J - K_s)) | X, Y, Z$ are known a priori.

To determine $v_*(X, Y, Z)$, we use a likelihood approach that models the full rate function $\lambda(O|\theta)$ that gives the number of stars as a function of all observables O of interest for a set of model parameters θ . These observables O are in this case $(\alpha, \delta, D, J, J - K_s)$ – we will use (X, Y, Z) and (α, δ, D) interchangeably because they are related by coordinate transformation, but will keep track of the Jacobian – and we can write

$$\begin{aligned} \lambda(O|\theta) &= \lambda(\alpha, \delta, D, J, J - K_s), \\ &= v_*(X, Y, Z|\theta) D^2 \cos \delta \\ &\times \rho_{\text{CMD}}(M_J, [J - K_s]_0 | X, Y, Z) S(J, J - K_s, \alpha, \delta), \end{aligned} \quad (1)$$

where we have assumed that the model parameters only affect v_* . In this decomposition, the factor $D^2 \cos \delta$ comes from the Jacobian of the transformation between (α, δ, D) and (X, Y, Z) .

An observed set of stars indexed by i is a draw from a Poisson process with rate function $\lambda(O|\theta)$ with the likelihood $\mathcal{L}(\theta)$ of the parameters θ describing the density law given by

$$\begin{aligned} \ln \mathcal{L}(\theta) &= \sum_i \ln \lambda(O_i|\theta) - \int dO \lambda(O|\theta), \\ &= \sum_i \ln v_*(X_i, Y_i, Z_i|\theta) - \int dD D^2 d\alpha d\delta \cos \delta v_*(X, Y, Z|\theta) \\ &\times \int dJ d(J - K_s) \rho_{\text{CMD}}(M_J, [J - K_s]_0 | X, Y, Z) \\ &\times S(J, J - K_s, \alpha, \delta), \end{aligned} \quad (2)$$

where in the second equation we have dropped terms that do not depend on θ . As in Bovy et al. (2016) we simplify this expression by defining the *effective selection function* $\mathbf{S}(\alpha, \delta, D)$ defined by

$$\begin{aligned} \mathbf{S}(\alpha, \delta, D) &\equiv \int dJ d(J - K_s) \rho_{\text{CMD}}(M_J, [J - K_s]_0 | X, Y, Z) \\ &\times S(J, J - K_s, \alpha, \delta), \end{aligned} \quad (3)$$

where $5 \log_{10}(D/10 \text{ pc}) = J - M_J - A_J | X, Y, Z$ and $[J - K_s]_0 = J - K_s - E(J - K_s) | X, Y, Z$. The ln likelihood then becomes

$$\begin{aligned} \ln \mathcal{L}(\theta) &= \sum_i \ln v_*(X_i, Y_i, Z_i|\theta) \\ &- \int dD D^2 d\alpha d\delta \cos \delta v_*(X, Y, Z|\theta) \mathbf{S}(\alpha, \delta, D). \end{aligned} \quad (4)$$

Unlike the selection function $S(J, J - K_s, \alpha, \delta)$ which depends on the survey's operations only (which parts of the sky were observed, for how long, etc.), the effective selection function $\mathbf{S}(\alpha, \delta, D)$ is a function of both the survey operations *and* the stellar population under investigation. Its usefulness derives from the fact that it encapsulates all observational effects due to selection and dust obscuration and turns the inference problem into a purely geometric problem. It directly gives the fraction of stars in a given stellar population that are observed by the survey in a given direction and at a

given distance. Like the survey selection function $S(J, J - K_s, \alpha, \delta)$, $\mathbf{S}(\alpha, \delta, D)$ takes values between zero (fully incomplete) and one (fully complete). Under the assumption that the CMD $\rho_{\text{CMD}}(M_J, [J - K_s]_0 | X, Y, Z)$ and the three-dimensional extinction map $(A_J, E(J - K_s)) | X, Y, Z$ are known (or at least fixed in the analysis), the effective selection function can be computed *once* for a given (survey and stellar population) pair.

To determine the best-fitting parameters $\hat{\theta}$ of a parametrized density law $v_*(X, Y, Z|\theta)$ one has to optimize the ln likelihood given above. This ln likelihood can be marginalized analytically over the overall amplitude of the density (the local normalization if you will); this is discussed in Bovy et al. (2016) and similar expressions would apply here if such a marginalization is desired.

2.2 Non-parametric binned density laws

Now suppose that one wants to determine the density $v_*(X, Y, Z)$ of a stellar population in a set of non-overlapping bins in (X, Y, Z) . The bins are given by a set $\{\Pi_k\}_k$ of rectangular functions that evaluate to unity within the domain of the bin and zero outside of it. The domain can have an arbitrary shape, but typically this would be an interval in each of X , Y , and Z or perhaps in R_{xy} and Z , where $R_{xy} = \sqrt{X^2 + Y^2}$. We can then write the density as

$$v_*(X, Y, Z|\theta) = \sum_k n_k \Pi_k(X, Y, Z), \quad (5)$$

where $\theta \equiv \{n_k\}_k$ is a set of numbers that give the density in each bin and that therefore parameterizes the density law.

The ln likelihood then becomes

$$\begin{aligned} \ln \mathcal{L}(\{n_k\}_k) &= \sum_i \ln \sum_k n_k \Pi_k(X_i, Y_i, Z_i) \\ &- \int dD D^2 d\alpha d\delta \cos \delta \sum_k n_k \Pi_k(X, Y, Z) \mathbf{S}(\alpha, \delta, D), \end{aligned} \quad (6)$$

which, because the $\{\Pi_k\}_k$ are a set of non-overlapping bins, can be simplified to

$$\begin{aligned} \ln \mathcal{L}(\{n_k\}_k) &= \sum_k \left[N_k \ln n_k \right. \\ &\left. - n_k \int dD D^2 d\alpha d\delta \cos \delta \Pi_k(X, Y, Z) \mathbf{S}(\alpha, \delta, D) \right], \end{aligned} \quad (7)$$

where N_k is the number of points i in the observed set that fall within bin k . We can maximize this likelihood for each n_k analytically and find best-fitting \hat{n}_k

$$\hat{n}_k = \frac{N_k}{\int dD D^2 d\alpha d\delta \cos \delta \Pi_k(X, Y, Z) \mathbf{S}(\alpha, \delta, D)}. \quad (8)$$

The denominator in this expression is known as the *effective volume*. Using the same symbol Π_k to denote the three-dimensional integration region and using $x = (X, Y, Z)$ and (α, δ, D) interchangeably because they are related through coordinate transformation, this can be written as the following simple expression

$$\hat{n}_k = \frac{N_k}{\int_{\Pi_k} d^3x \mathbf{S}(\alpha, \delta, D)}. \quad (9)$$

Thus, the effective volume corresponding to a given spatial region Π_k is the spatial integral of the effective selection function over Π_k .

We can then define the *effective volume completeness* $\Xi(\Pi_k)$ of the spatial region Π_k as

$$\Xi(\Pi_k) = \frac{\int_{\Pi_k} d^3x \mathbf{S}(\alpha, \delta, D)}{\int_{\Pi_k} d^3x}, \quad (10)$$

where $\int_{\Pi_k} d^3x = V(\Pi_k)$ is simply the actual geometric volume of Π_k . Because $\mathbf{S}(\alpha, \delta, D)$ is a function bounded by zero and one, the effective volume completeness $\Xi(\Pi_k)$ also takes values between zero and one. In terms of $\Xi(\Pi_k)$, equation (9) becomes

$$\hat{n}_k = \frac{N_k}{\Xi(\Pi_k) V(\Pi_k)} = \frac{1}{\Xi(\Pi_k)} \frac{N_k}{V(\Pi_k)}. \quad (11)$$

This expression makes sense, because for a complete sample $\mathbf{S}(\alpha, \delta, D) = 1$, such that $\Xi(\Pi_k) = 1$ and this expression simplifies to the number divided by the volume of the bin, the standard way to compute a number density.

From the second derivative of the ln likelihood, we find the uncertainty on the \hat{n}_k

$$\sigma_{\hat{n}_k} = \frac{\hat{n}_k}{\sqrt{N_k}}. \quad (12)$$

3 THE TGAS COMPLETENESS FOR DIFFERENT STELLAR POPULATIONS

From the discussion above, it is clear that for a given survey and a given stellar population, the completeness functions of interest are (i) the effective selection function $\mathbf{S}(\alpha, \delta, D)$ and (ii) the effective volume completeness $\Xi(\Pi_k)$. In this section, we compute these functions for different stellar types along the main sequence and along the giant branch using the *TGAS* selection function determined in Appendix A. These functions will give a sense of how *TGAS* samples the extended solar neighbourhood for a given stellar type.

3.1 Definitions of stellar types

The near-infrared CMD for stars with well-determined parallaxes ϖ in *TGAS* is displayed in Fig. 1. ‘Well-determined parallaxes’ for the purpose of this figure means (i) $\varpi/\sigma_\varpi > 10$ if $M_J < 0$, (ii) $\varpi/\sigma_\varpi > 20$ for $M_J > 5$, and (iii) $\varpi/\sigma_\varpi > 20 - 2(M_J - 5)$ for $0 < M_J < 5$, with M_J computed based on the *TGAS* ϖ without correcting for extinction. These cuts are chosen to have a relatively well-populated upper main sequence and giant branch, because simple cuts on ϖ/σ_ϖ tend to select few intrinsically bright, and thus typically distant, stars. We use stars contained within the darkly shaded region as a sampling $(M_J, [J - K_s]_0)_j$ of the intrinsic CMD $\rho_{\text{CMD}}(M_J, [J - K_s]_0)$, which we assume to be independent of position. This is a reasonable assumption for the $D \lesssim 1$ kpc probed by *TGAS*. The darkly shaded region is defined by a shifted and stretched version of the mean dwarf stellar locus from Pecaut & Mamajek (2013) and of the giant locus described below.

Along the main sequence, we define stellar types everywhere in this paper using the mean dwarf stellar locus from Pecaut & Mamajek (2013),¹ displayed as a grey curve in Fig. 1. Thus, we define A dwarfs as those stars along the main sequence with $J - K_s$ colours between the colour of A0V and A9V stars according to the

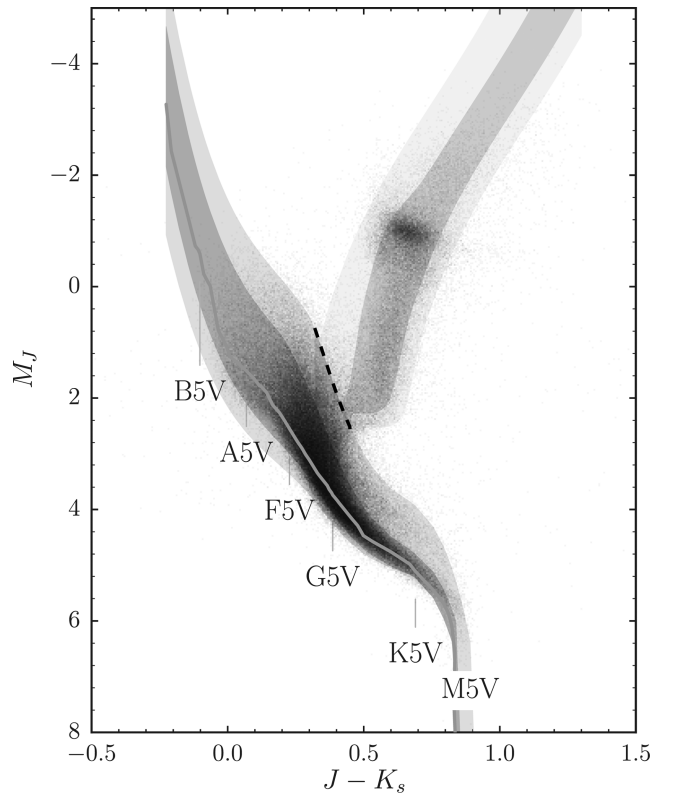


Figure 1. Near-infrared CMD for *TGAS* stars. The light grey line displays the mean dwarf stellar locus from Pecaut & Mamajek (2013). The lightly shaded area shows how we select main-sequence and giant stars for the purpose of star counts; the darkly shaded area displays the more stringent cuts that we use to determine the absolute magnitude distribution of different stellar types. The dashed line gives the assumed separation between the main sequence and the giant branch. Major stellar types along the main sequence are labelled.

stellar locus and similarly for F, G, and K stars. For M stars, we only go as red as the colour of M5V dwarfs ($[J - K_s]_0 = 0.89$). In Section 4, we further subdivide each stellar type into subtypes A0V, A1V, etc. For those cases, the $J - K_s$ boundaries are located half-way between the stellar subtype in question and the adjoining subtypes. For example, for A1V the boundary goes from half-way between A0V and A1V to half-way between A1V and A2V. The sampling $(M_J, [J - K_s]_0)_j$ for a given stellar type then consists of those stars in the correct colour range that fall within the darkly shaded region of Fig. 1. We always limit this sample to 1000 stars for computational reasons.

We proceed similarly to define different types of giants. As a fiducial giant locus, we use a solar metallicity ($Z = 0.017$) PARSEC isochrone with an age of $10^{0.8}$ Gyr (Bressan et al. 2012). For simplicity, we define different types of giants using a simple cut on M_J : (i) ‘subgiants’ for $1 < M_J < 4$, (ii) ‘lower RGB’ for $-0.5 < M_J < 1$, (iii) ‘red clump’ (RC) for $-1.5 < M_J < -0.5$, and (iv) ‘upper RGB’ for $-4 < M_J < -1.5$. In Section 5 below, we will further subdivide these types into $\Delta M_J = 0.25$ mag bins. Similar to the main-sequence stars above, a sampling $(M_J, [J - K_s]_0)_j$ for a given giant type then consists of those stars in the correct M_J range that fall within the darkly shaded region to the right of the dashed line in Fig. 1. This selection of giants largely avoids the asymptotic giant branch.

¹ Specifically, we use version 2016.08.21 downloaded from http://www.pas.rochester.edu/~emamajek/EEM_dwarf_UBVIJHK_colors_Teff.txt.

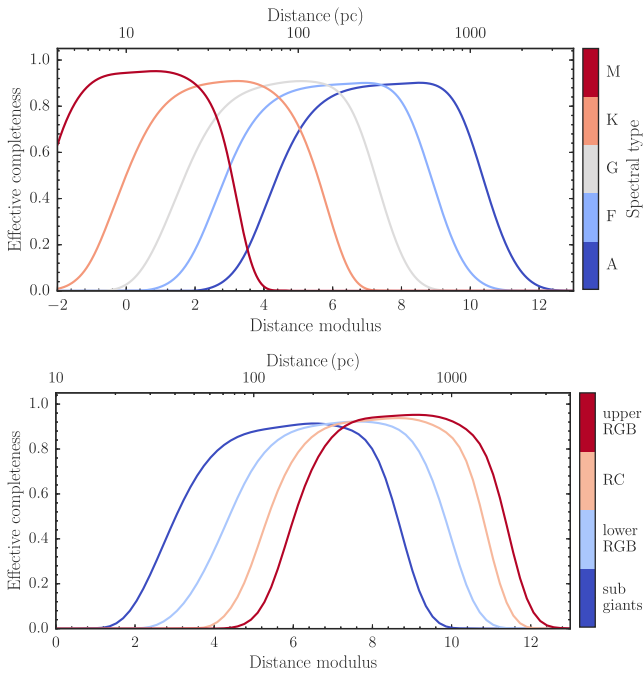


Figure 2. Effective selection function (or ‘effective completeness’) for different stellar types in *TGAS* as a function of distance, assuming that extinction is negligible.

3.2 Effective selection function for different stellar types in *TGAS*

With the definitions of different stellar types from the previous subsection, we compute the effective selection function $\mathfrak{S}(\alpha, \delta, D)$ for different stellar types. In particular, we use the sampling $(M_j, [J - K_s]_0)_j$ from $\rho_{\text{CMD}}(M_j, [J - K_s]_0)$ for each stellar type to approximate equation (3) as a Monte Carlo integration

$$\begin{aligned} & \mathfrak{S}(\alpha, \delta, D) \\ & \equiv \int dJ d([J - K_s]) \rho_{\text{CMD}}(M_j, [J - K_s]_0 | X, Y, Z) \\ & \quad \times S(J, J - K_s, \alpha, \delta), \\ & \approx \sum_j S(M_{j,j} + \mu + A_j, [J - K_s]_{0,j} + E(J - K_s), \alpha, \delta), \end{aligned} \quad (13)$$

where we substitute $(J, J - K_s) = (M_{j,j} + \mu + A_j, [J - K_s]_{0,j} + E(J - K_s))$ in $S(J, J - K_s, \alpha, \delta)$. In this equation, $\mu = 5 \log_{10}(D/10\text{pc})$ is the distance modulus and we have suppressed the dependence of the extinction map ($A_j, E(J - K_s)$) on (α, δ, D) . In the absence of extinction, the effective selection function becomes

$$\mathfrak{S}(\alpha, \delta, D) \approx \sum_j S(M_{j,j} + \mu, [J - K_s]_{0,j}, \alpha, \delta). \quad (14)$$

Because our *TGAS* selection function $S(J, J - K_s, \alpha, \delta)$ does not depend on (α, δ) within the region of the sky over which it is defined, this is a one-dimensional function of distance.

The effective selection function in the absence of extinction is shown for different stellar types in Fig. 2. Along the main sequence, the overall trend is that later types of stars can be seen out to a smaller distance than earlier types of stars. This is because of two reasons: not only are later type dwarfs intrinsically fainter, but the *TGAS* selection function also has a brighter faint-end cut-off for redder, late-type stars (see Fig. A10 in the appendix). On the other hand, the *TGAS* selection function has a slightly higher plateau value at

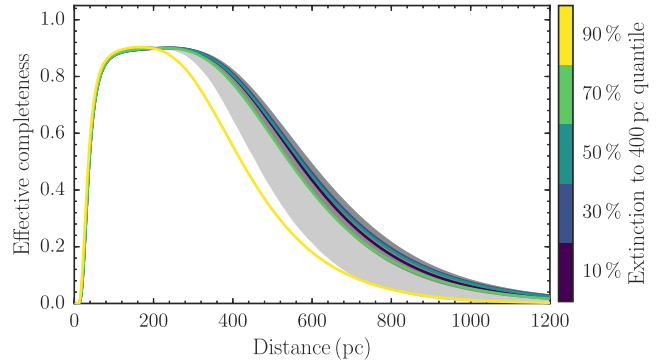


Figure 3. Effect of the three-dimensional dust extinction on the effective completeness. This figure displays the effective completeness of F dwarfs in *TGAS* as a function of distance in regions with different amounts of extinction. The coloured curves show the effective completeness in 3.36 deg^2 sky regions at five quantiles of the distribution of the mean extinction to 400 pc. The dark and light grey bands display the 68 per cent and 95 per cent lower limits of the completeness over the sky. The effect of extinction is small over the majority of the sky.

intermediate magnitudes for redder stars, which has the effect that the M-dwarf effective selection function is slightly higher than for earlier types at its peak. The lower distance limit results from the bright cut-off of the *TGAS* selection function stemming from the exclusion of the brightest ($G \lesssim 6$) stars in *TGAS*. For A, F, and G dwarfs, this causes a hole around the location of the Sun for these stars extending up to about 100 pc for A stars.

The effective selection function for different types of giants in Fig. 2 behaves similarly to that of the dwarfs. Intrinsically brighter giants can be seen out to larger distances, but not much larger distances, because the intrinsically brighter (in the near-infrared) giants on the upper RGB are also redder, where the *TGAS* selection function cuts off at brighter magnitudes. For both early-type dwarfs and luminous giants, the effective selection function becomes small around 2 kpc. The bright cut-off of the *TGAS* selection function again causes a hole around the location of the Sun of ≈ 50 to ≈ 200 pc for giants depending on their luminosity.

The curves in Fig. 2 are for the case of zero extinction. For the intrinsically brighter stellar types that extend out to $\gtrsim 1$ kpc, extinction has important effects. Because the extinction varies as a function of three-dimensional position, the effective selection function computed using equation (13) becomes a function of (α, δ, D) . We compute the extinction using the combined extinction model from Bovy et al. (2016), which merges the three-dimensional extinction maps from Marshall et al. (2006), Green et al. (2015), and Drimmel, Cabrera-Lavers & López-Corredoira (2003). These maps are combined in this order in the case of overlap to create a full-sky three-dimensional extinction map (see the appendix of Bovy et al. 2016 for full details). In what follows, we use this map at its full resolution, which varies between $\approx 4'$ and $\approx 20'$.

The effect of extinction on the zero-extinction curves in Fig. 2 is displayed in Fig. 3, focusing on F dwarfs. The effect of extinction is mainly to lower the distance out to which a stellar population can be observed. A secondary effect is that the peak of the effective selection function can become higher, because of the higher completeness to redder stars in *TGAS*, but this is a minor effect. The narrow dark grey region contains 68 per cent of the part of the sky for which we have determined the *TGAS* selection function; the light grey region contains 95 per cent. To give another sense of this, the coloured lines are lines of sight (in $N_{\text{side}} = 32$ HEALPix pixels)

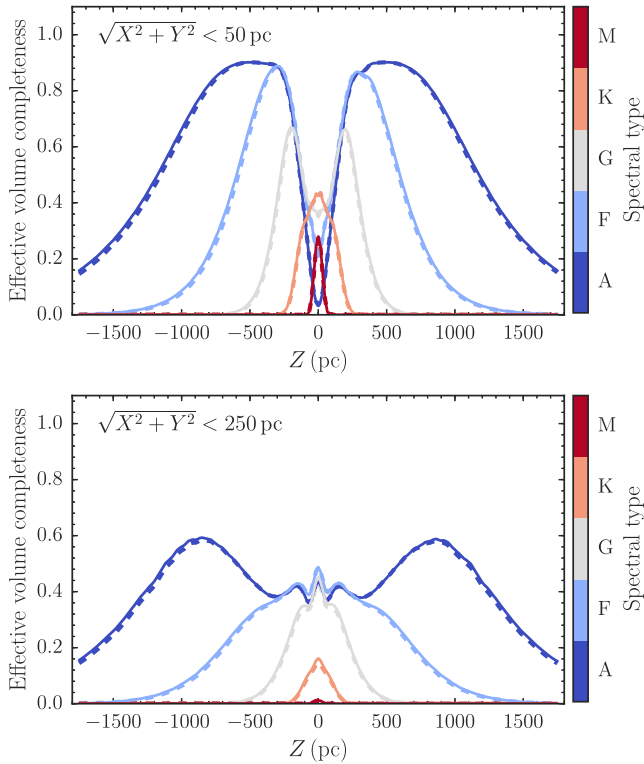


Figure 4. Effective volume completeness for different stellar types along the main sequence as a function of vertical distance from the Sun. The completeness is computed in cylinders centred on the Sun perpendicular to the (X, Y) plane with a radius of $R_{xy} = 50$ and 250 pc in the top and bottom panels, respectively, and in Z slices with a width of 50 pc. The solid curves assume zero dust extinction, while the dashed lines use a model for the three-dimensional dust distribution; the effects of extinction are small. *TGAS*'s bright limit causes a hole in the narrow cylinder for early-type dwarfs. The effective completeness has small-scale structure that needs to be taken into account when using *TGAS* to determine the underlying stellar density profile of different stellar types.

at the 10–90th quantile of the distribution of the mean extinction to 400 pc. Thus, the effect of extinction is overall small, except for the about 10 per cent of the sky with high extinction, located near the Galactic plane.

3.3 Effective volume completeness maps for *TGAS*

Similar to the effective selection function $\mathfrak{S}(\alpha, \delta, D)$, we can compute the effective volume completeness $\Xi(\Pi_k)$ for different kinds of volumes Π_k and for different types of stars. The effective volume completeness in cylindrical regions with height 50 pc centred on $(X, Y) = (0, 0)$ with the cylinder's axis parallel to the Z -axis of the heliocentric coordinate frame is shown in Fig. 4 for different stellar types along the main sequence. The top panel considers a narrow cylinder with a radius of $R_{xy} = 50$ pc, the bottom panel a broader cylinder with a radius of $R_{xy} = 250$ pc. Because the effective selection function of giants in Fig. 2 closely resembles that of earlier type main-sequence stars, the effective volumes for giants are similar to those of A, F, and G dwarfs and are not shown in Fig. 4.

Because of the bright cut-off of *TGAS*, A, F, and G dwarfs have a hole in their effective volume centred on the Sun (see above) for the narrow cylinder. This hole is absent for the broader cylinder, because it gets filled in by stars at $|Z| \approx 0$, but with $(X, Y) = \mathcal{O}(100, 100)$ pc. Because we only determined the *TGAS* selection

function over 48 per cent of the sky, the broader cylinder has a complicated effective volume as a function of Z for A and F stars. The effective volume for K dwarfs is small beyond a few 100 pc and M dwarfs are only sampled substantially by *TGAS* out to about 50 pc.

The dashed curves in Fig. 4 represent the effective volume when taking the full three-dimensional distribution of interstellar extinction into account, while the solid curves assume that there is no extinction. It is clear that extinction only has a very minor, percent-level effect on the effective volume in vertical slices near the Sun.

To get a sense of how *TGAS* samples stars of different types over the full three-dimensional volume around the Sun, we compute the effective volume completeness $\Xi(\Pi_k)$ for cubic volumes in (X, Y, Z) with a volume of $(100 \text{ pc})^3$. This effective volume completeness is displayed for different main-sequence stellar types in vertical slices in Fig. 5 and in slices in X in Fig. 6. The same for different types along the giant branch is shown in Figs 7 and 8. These effective volume completenesses take the full three-dimensional extinction map into account.

These maps of the *TGAS* volume completeness give a direct sense of the volume probed by different stellar types, with early main-sequence stars sampling a substantial fraction out to ≈ 2 kpc out of the plane and ≈ 1 kpc in the plane and late-type dwarfs only extending out to ≈ 50 pc. The intrinsically bright giants ($M_J \approx -2.5$) extend about as far as A dwarfs.

It is clear from these completeness maps that the *TGAS* completeness is complex, because of the patchy nature of the ‘good’ *TGAS* footprint over which we determined the selection function and because of the three-dimensional distribution of dust. Even if the remaining 52 per cent of the sky were included in the selection function, the volume completeness would remain complex, because the raw *TGAS* completeness is lower and complicated in this 52 per cent of the sky. These completeness maps need to be taken into account in any investigation using *TGAS* for which the stellar density or the manner in which a stellar-population samples the local volume matters. Tools to compute the effective completeness and the effective volume completeness for a given stellar type are available in the `gaia_tools.select.tgasEffectiveSelect` class in the `gaia_tools` package available at https://github.com/jobovy/gaia_tools.

4 STELLAR DENSITY LAWS FOR MAIN-SEQUENCE STARS

We now combine the method for determining non-parametric, binned stellar densities from Section 2.2 with the determination of the effective volume completeness from Section 3 to determine the stellar density and its vertical dependence for different stellar types along the main sequence. In Section 4.1, we test the effective volume completeness by directly comparing simple models for the stellar density of various types of stars combined with the effective volume completeness with the observed number counts in *TGAS*. In Section 4.2, we determine the stellar density and its vertical dependence in narrow Z bins and fit these with simple analytic profiles. Section 4.3 focuses on the measurement of the mid-plane stellar densities and its implications for the present-day mass function, the star formation history, and the density of stellar remnants in the solar neighbourhood. We postpone a discussion of the Sun's offset from the mid-plane defined by different types of stars to Section 6, where we discuss the measured offset for both main-sequence stars and giants.

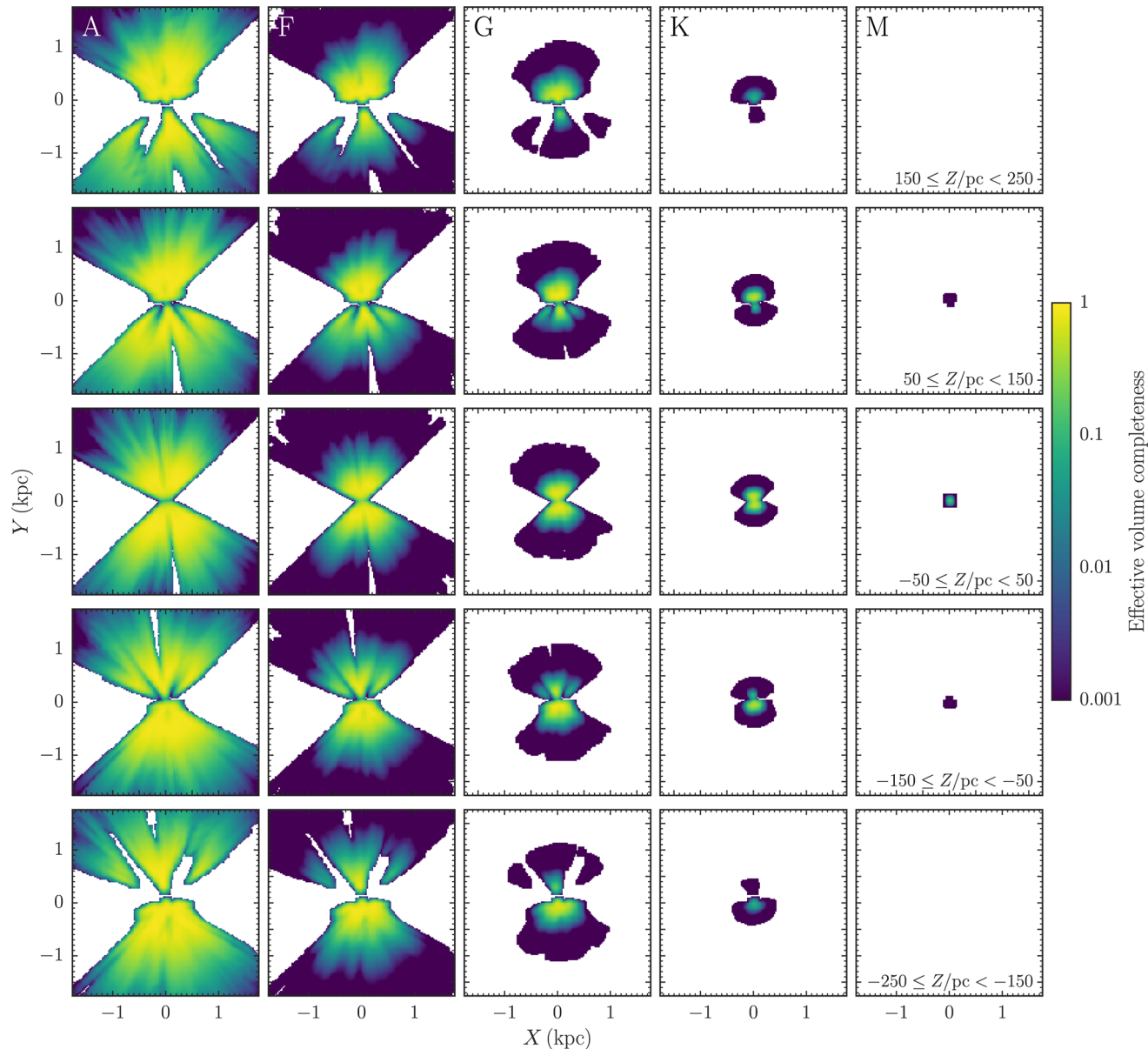


Figure 5. Effective volume completeness for different stellar types along the main sequence in $(100 \text{ pc})^3$ boxes. The volume completeness is displayed as a function of (X, Y) in five Z slices. The incomplete, white parts for A and F stars are a result of the sky cut (mostly aligned with the ecliptic, see Appendix A). The volume covered going from A to M dwarfs decreases rapidly, both because later type dwarfs are intrinsically fainter and because TGAS's completeness drops off at brighter magnitudes for red stars than for blue stars.

In this and the subsequent section, we count as stars those TGAS sources that fall within the lightly shaded region shown in Fig. 1, including the overlap with the darkly shaded region. This light-shaded region is a shifted and stretched version of the mean dwarf stellar locus from Pecaut & Mamajek (2013) and of the giant locus described above, similar to the dark-shaded region discussed in Section 3.1. It is designed, by hand, to encompass the vast majority of stars that are plausibly part of the dwarf and giant sequences, without including outliers. Because there are only very few stars outside of the light-shaded area and all we use are the number counts of stars, none of our results are significantly affected by changes to this area. We estimate distances simply as inverse parallaxes and only consider stars out to distances of $444 \text{ pc} = 0.2/[0.45 \text{ mas}]$. Because the parallax uncertainties in the part of the sky that we consider are typically $< 0.45 \text{ mas}$ (see Appendix A), these stars typically have

relative parallax uncertainties better than 20 per cent, small enough that the distance estimate from the inverse parallax is not strongly biased (Bailer-Jones 2015). We only count stars up to $|Z| = 412.5 \text{ pc}$ and to a maximum $\sqrt{X^2 + Y^2} < 250 \text{ pc}$, so this distance cut only affects these very furthest bins for the most luminous stars.

Because the effects of three-dimensional extinction are small (see discussion in Sections 3.2 and 3.3), yet computationally laborious to compute, we ignore extinction in this section. We have performed the analysis described in this section taking into account the three-dimensional dependence of extinction for the main spectral classes (all A dwarfs, all F dwarfs, etc.) and find differences of only 1–2 per cent in the stellar density distributions and inferred parameters of the vertical density profile compared to assuming no extinction. These are a factor of a few or more smaller than our statistical uncertainties.

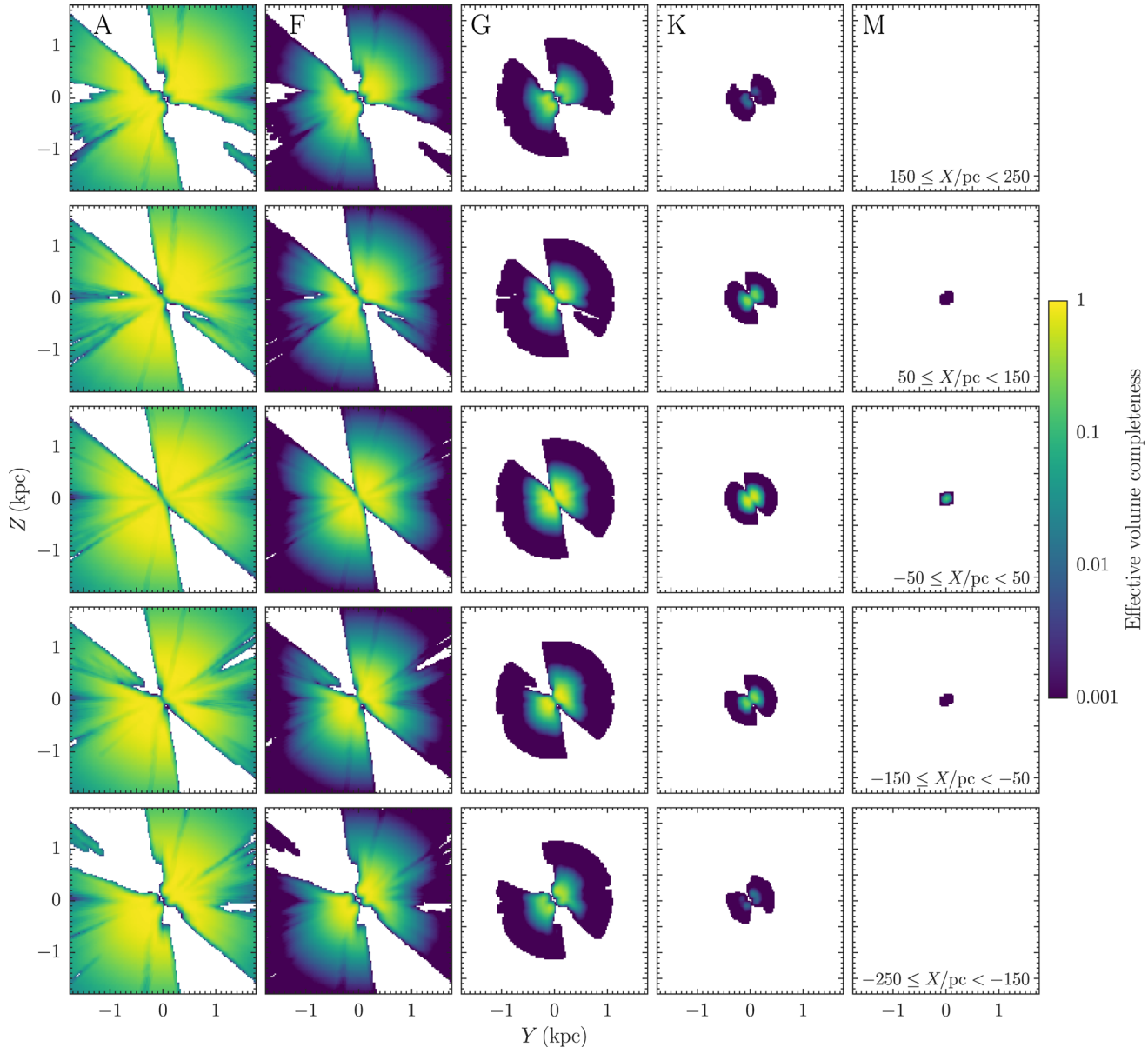


Figure 6. Like Fig. 5, but for the volume completeness in the (Y, Z) plane in five X slices. Because extinction is smaller looking out of the $Z = 0$ plane, the completeness remains high even at high Z for A and F stars.

4.1 Forward modelling of the observed star counts

Before discussing our determination of the underlying stellar density profiles of main-sequence stars, we test how well the observed star counts for different stellar types are represented by the effective volume completeness that we compute based on the raw *TGAS* selection function from Appendix A combined with the model for the CMD of different stellar types from Section 3.

The observed number counts of late K dwarfs (K5V–K9V) in a 100 pc wide cylinder centred on the Sun in 25 pc wide bins in Z are displayed in Fig. 9. From the discussion above in Section 3.3, it is clear that late K dwarfs can only be observed at relatively high completeness out to $|Z| \lesssim 100$ pc. From our prior understanding of the vertical density profile of late K dwarfs, we know that the scaleheight of these typically old stars is $\gg 100$ pc (e.g. Jurić et al. 2008) and the vertical density profile should thus be close to constant within the observed *TGAS* volume. Therefore, we expect the

observed number counts to largely reflect the completeness of the survey rather than the underlying stellar density profile. If the underlying density is constant, then the counts in equal-volume bins are proportional to the effective volume completeness: $N_k \propto \Xi(\Pi_k)$ (equation 11). The blue curve in Fig. 9 shows the vertical dependence of the effective volume completeness, re-scaled to the median of the three central points (to fix the proportionality constant). This simple ‘model’ matches the observed number counts well.

To compare the observed number counts to those predicted by the effective volume completeness for stars that are more luminous or younger than late K dwarfs, we need to model the underlying density profiles. Below, we fit simple sech^2 profiles to the binned stellar density laws of different stellar types. Fig. 10 compares the observed number counts for early F dwarfs (F0V–F4V) and for RC stars (discussed in more detailed in Section 5 below) with underlying stellar densities \hat{n}_k fit as sech^2 profiles and multiplied by the

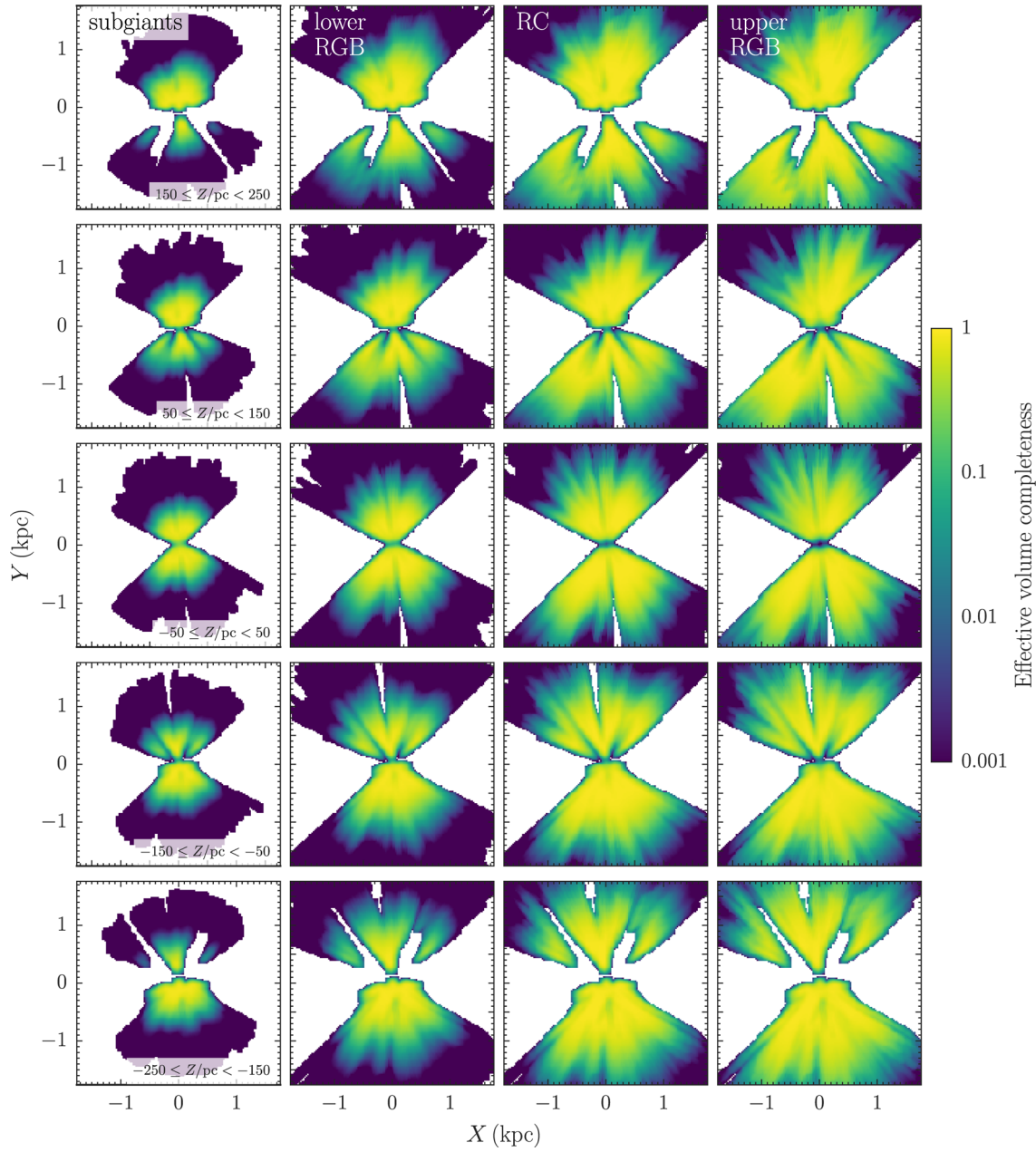


Figure 7. Like Fig. 5, but for stars along the giant branch.

effective volume ($N_k = \hat{n}_k \times [\Xi(\Pi_k) V(\Pi_k)]$ from equation 11). It is clear that these models fit the observed number counts well: the vertical dependence and the dips near $Z = 50$ pc are the same in the model and the observed number counts. The dips are caused by the geometry of the ‘good’ part of the sky.

We conclude that we can successfully model the observed number counts of stars in *TGAS* using the effective volume completeness determined in Section 3.

4.2 Binned stellar densities along the main sequence

The binned vertical stellar density of stellar subtypes from A0V to K9V are displayed in Fig. 11. To account for the fact that luminous A dwarfs can be seen to much larger distances than faint K dwarfs, these vertical densities are determined in 25 pc wide ranges in Z in a cylinder that extends out to $R_{xy} = 250$ pc for A dwarfs, 200 pc

for F dwarfs, 150 pc for G dwarfs, and 100 pc for K dwarfs. We do not consider M dwarfs, because the volume over which *TGAS* has relatively high completeness to M dwarfs is very small. While we determine absolute stellar densities, we shift the profiles in the y -direction in this figure to better display the vertical dependence. For each stellar type, we only show bins with (i) more than four stars, (ii) effective volume completeness larger than 3 per cent of the maximum effective volume completeness for the stellar type in question, and (iii) effective volume completeness larger than 1 part in 10^5 , except for the $Z = 0$ bin. These cuts are designed to weed out bins where our stellar densities are highly noisy.

It is clear that the vertical profiles in Fig. 11 broaden significantly when going from the earliest types of A dwarfs to later G and K dwarfs. By G5V, *TGAS* does not extend far enough to see a substantial decrease in the stellar density with vertical distance from the Sun. By K5V, the volume over which *TGAS* has significant

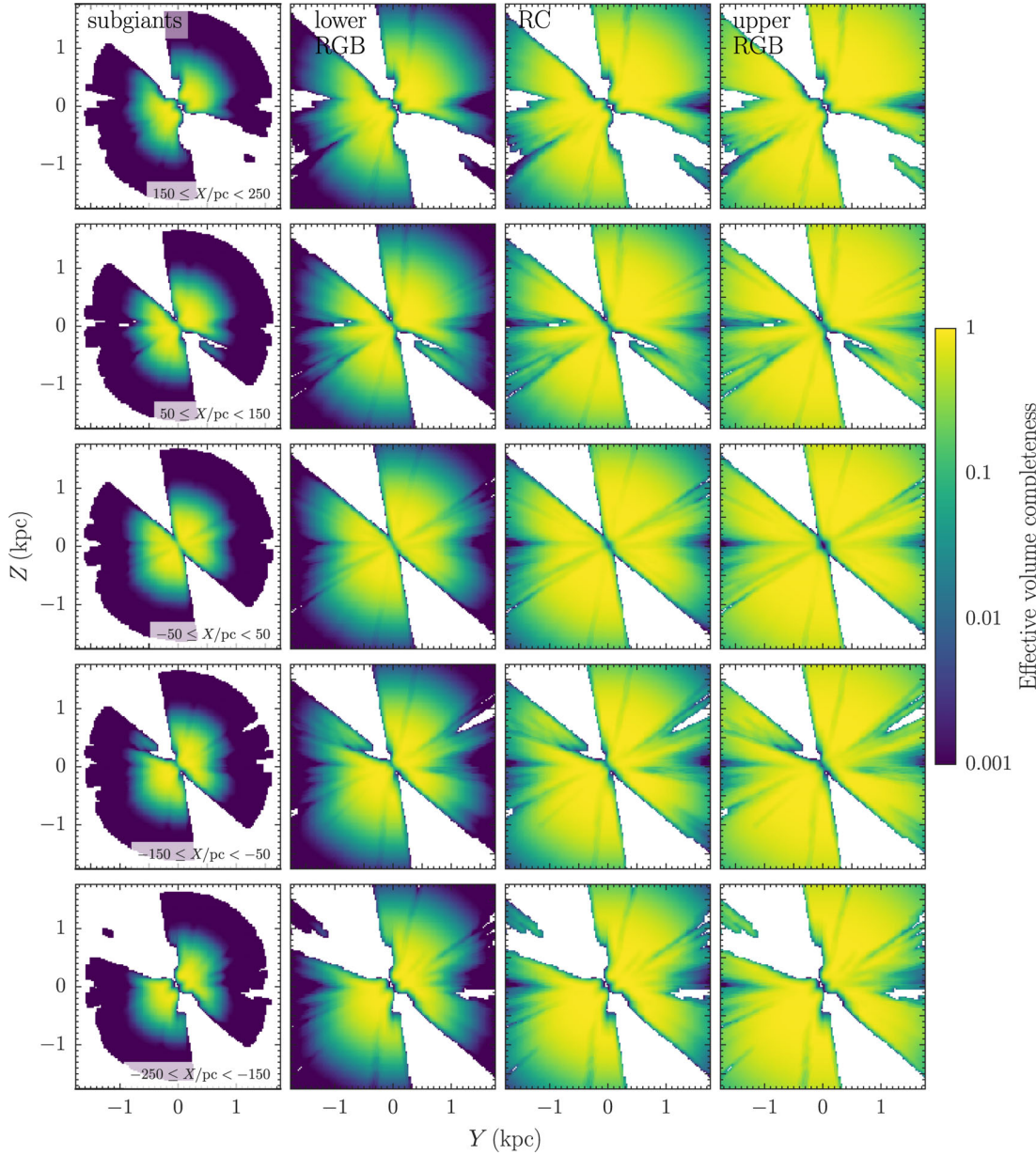


Figure 8. Like Fig. 7, but for the volume completeness in the (Y, Z) plane in five X slices.

completeness has become so small that it is difficult to measure the density at all.

We fit each stellar type's number density profile by minimizing the χ^2 deviation between the observed $\hat{n}_k \pm \sigma_{\hat{n}_k}$ and a model composed of two sech^2 profiles

$$\nu_*(Z) = n \left[(1 - \alpha) \text{sech} \left(\frac{Z + Z_\odot}{2z_d} \right)^2 + \alpha \text{sech} \left(\frac{Z + Z_\odot}{2z_{d,2}} \right)^2 \right], \quad (15)$$

where n is the mid-plane density, z_d is the scaleheight of the main sech^2 component, Z_\odot is the Sun's offset from the mid-plane, α is the fraction of the mid-plane density that is part of the second sech^2 , and $z_{d,2}$ is the scaleheight of the second sech^2 component, constrained to be larger than z_d . This $z_{d,2} \gg 1$ kpc in almost all cases, such that the second sech^2 profile is essentially a constant density. The second component typically has a small amplitude α , especially for

the earlier types (for later types, it becomes degenerate with the first component, because these types' densities are close to constant). Thus, the measured number density profiles are well represented by sech^2 profiles within $|Z| \lesssim 4z_d$ or $|Z| < 400$ pc (if $4z_d > 400$ pc). The fit are shown as blue curves in Fig. 11; the grey band displays the 68 percent confidence region obtained by MCMC sampling of the likelihood defined as $\exp(-\chi^2/2)$.

The parameters for each stellar type together with their uncertainties are given in Table 1. We list the mean colour, absolute magnitude in V and J , and the mass of each type determined from the dwarf locus from Pecaut & Mamajek (2013). We also give the derived quantities dn/dM_V (the luminosity function), dn/dM (the mass function), and the mid-plane mass density $\rho(>M)$ of stars with masses down to that of the stellar type in question. For types later than K4V, we are not able to determine reliable parameters because of the lack of data (see Fig. 11); for types later than G3V, we are unable to determine the scaleheight because the distance out

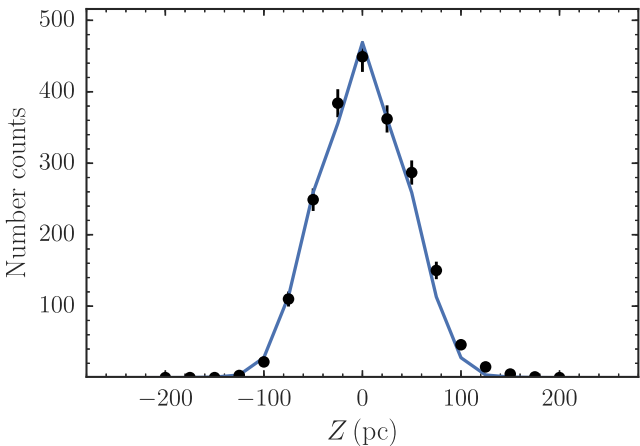


Figure 9. *TGAS* number counts of late K dwarfs (K5V–K9V, see Section 3.1) in a cylinder with radius $R_{xy} = 100$ pc in 25 pc wide bins in Z . The blue curve is the effective volume completeness scaled to the number counts. Because the intrinsic density distribution of late K dwarfs is essentially constant within $-100 \text{ pc} < Z < 100 \text{ pc}$, the number counts should basically reflect the volume completeness, which is indeed what we find.

to which these stars can be seen in *TGAS* is too small compared to their scaleheight.

The luminosity function dn/dM_V is shown in Fig. 12. We compare the luminosity function to that determined by Reid et al. (2002) from a volume complete sample within 25 pc from the Sun. The agreement between these two determinations is good; importantly, they are essentially based on non-overlapping volumes, because for G dwarfs and earlier types, *TGAS* only starts observing stars at distances greater than about 25 pc. This good agreement is partly due to the fact that we find that the Sun is at the mid-plane of the density of A and F stars (the measured Solar offsets using different stellar types are displayed in Fig. 19 below and discussed in more detail together with the equivalent measurements for giants in Section 6). If this was not the case, the 25 pc volume of Reid et al. (2002) would be offset from the mid-plane by half a scaleheight. The new determination based on *TGAS* data has much higher resolution in absolute magnitude than Reid et al. (2002), which has $\Delta M_V = 1$ compared to typical $\Delta M_V \approx 0.15$ here (of course, Reid et al. 2002 extend down to $M_V = 20$, while we are limited to $M_V \lesssim 7.5$).

The scaleheight for different stellar types is shown in Fig. 13 as a function of their main-sequence lifetime τ , computed as in Reid et al. (2002)

$$\log_{10} \tau(M) = 1.015 - 3.491 \log_{10} M + 0.8157 (\log_{10} M)^2. \quad (16)$$

Stars of a given stellar type will largely be younger than this age. The scaleheight rises gradually from ≈ 50 pc for A dwarfs to ≈ 100 pc for late F dwarfs and larger for older G dwarfs. The scaleheight of young populations of stars is less than half of that of the atomic and molecular hydrogen (McKee et al. 2015), but similar to that of young open clusters (≈ 50 –75 pc, e.g. Bonatto et al. 2006; Buckner & Froebrich 2014; Joshi et al. 2016) and of OB stars (≈ 50 pc, Reed 2000).

4.3 The mass function and star formation history of the solar neighbourhood

Using a relation for the mass as a function of stellar type along the main sequence, we can translate the luminosity function of Fig. 12 into a mass function dn/dM . We use masses for stellar types derived

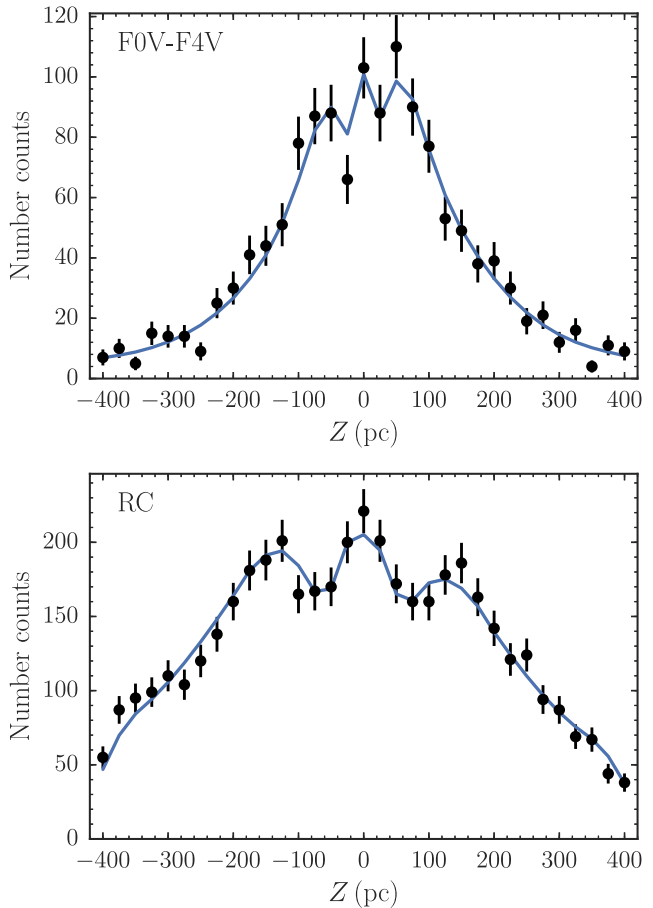


Figure 10. *TGAS* number counts of early F dwarfs (top) and of RC stars (bottom) in a cylinder with radius $R_{xy} = 100$ and 250 pc for F dwarfs and RC giants, respectively (see Section 3.1 for the definition of these subsamples). The blue curve displays the results from a fit of the underlying vertical stellar density with a sech^2 profile multiplied with the effective volume. The agreement between the number counts and the model is good.

from the dwarf mean stellar locus from Pecaut & Mamajek (2013). The resulting mass function is shown in Fig. 14. This function gives the mass density at the mid-plane in units of numbers of stars per solar mass and cubic parsecs. This is the present-day mass function. For long-lived stars this should reflect the IMF, while for short-lived stars the present-day mass function results from the combination of the IMF, stellar evolution, and kinematic heating. Our latest-type stars for which we can measure reliable mid-plane densities (K2V–K4V) are long-lived enough to trace all mass formed over the history of the disc (e.g. Bressan et al. 2012) and thus reflect the IMF for these types. Therefore, we anchor IMF models to the observed dn/dM of these populations. In particular, we employ the lognormal and exponential IMF models from Chabrier (2001) and the broken power-law IMF model from Kroupa (2001). The range spanned by these three IMFs when anchored to the K dwarfs (using the median proportionality constant) is shown as the grey band in Fig. 14.

We fit the high-mass end of the mass function using a power law and find

$$\frac{dn}{dM} = 0.016 \left(\frac{M}{M_\odot} \right)^{-4.7} M_\odot^{-1} \text{ pc}^{-3}, \quad M > 1 M_\odot. \quad (17)$$

This can be compared to the mass function obtained by Scalo (1986), who finds $dn/dM = 0.019 (M/M_\odot)^{-5.4} M_\odot^{-1} \text{ pc}^{-3}$; these differ by less than 25 per cent within the relevant mass range. Combining the

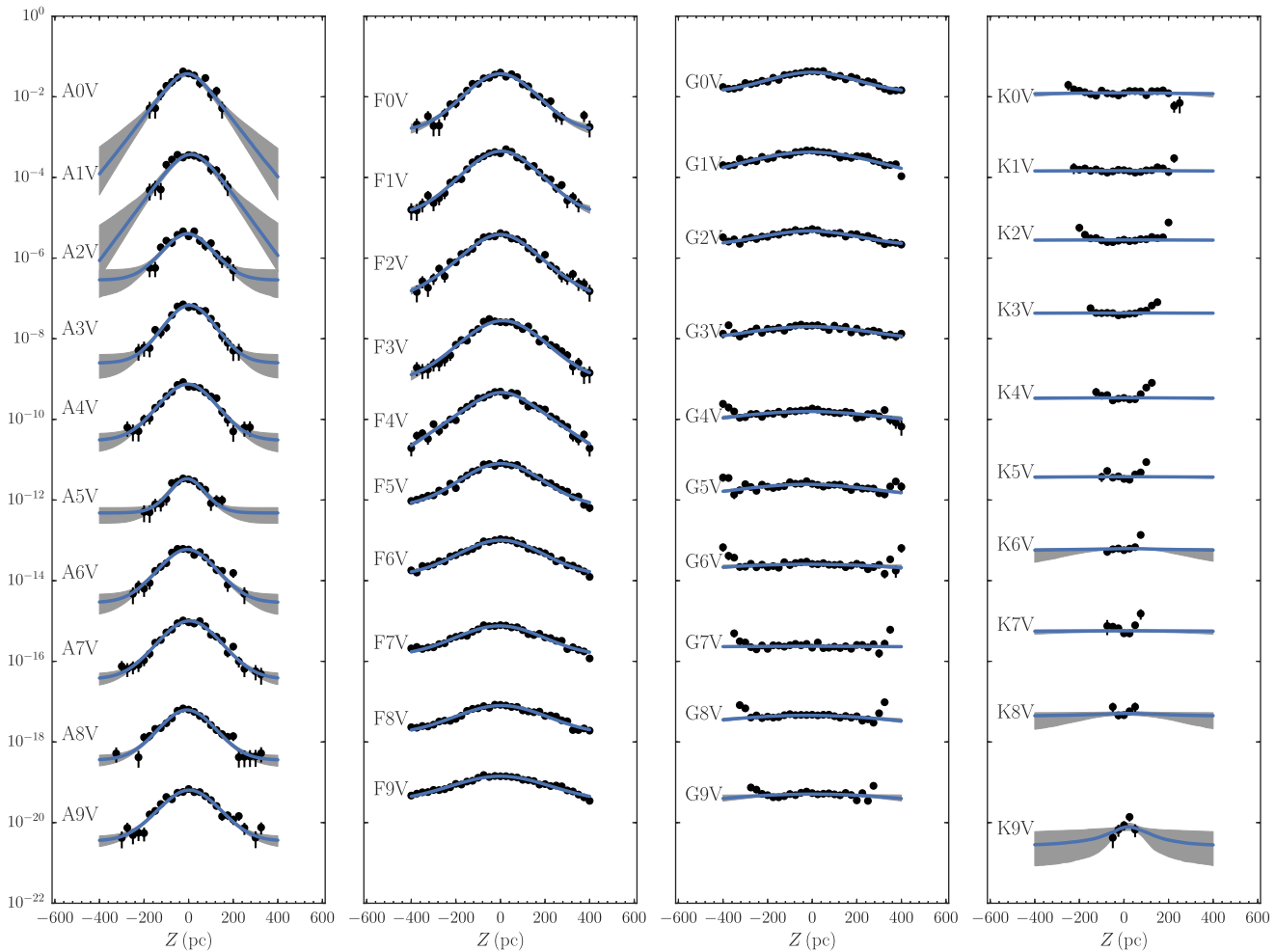


Figure 11. Vertical number density profiles of main-sequence stars of different stellar types. The black dots with uncertainties (mostly too small to see) are the data (*TGAS* number counts/effective volume), the blue curve is a sech^2 fit and the grey band is the 68 per cent uncertainty range of the sech^2 model. The profiles have been arbitrarily shifted in the y -direction. The vertical density flattens near the mid-plane for all stellar types and broadens as one moves from earlier to later stellar types. At later K dwarfs, the density becomes difficult to measure because of *TGAS*'s incompleteness.

power-law high-mass mass function at $M > 1 M_\odot$ with the IMF fit to the K dwarfs at $M \leq 1 M_\odot$, we can compute the total mid-plane density of main-sequence stars. This is

$$\rho_*^{\text{MS}} = 0.040 \pm 0.002 M_\odot \text{ pc}^{-3}, \quad (18)$$

where the uncertainty includes a contribution from the uncertainty in the raw *TGAS* selection function for K dwarfs. As shown in Table 1, only $0.01 M_\odot \text{ pc}^{-3}$ of this is directly determined from our stellar density measurements and the rest is an extrapolation down to $M = 0.08 M_\odot$ (assumed here to be the smallest mass above which core-hydrogen-burning occurs). This is in good agreement with previous determinations, e.g. the measurement of $\rho_*^{\text{MS}} = 0.036 \pm 0.004 M_\odot \text{ pc}^{-3}$ from McKee et al. (2015) based in large part on the measurements from Reid et al. (2002).

Above $1 M_\odot$, the difference between the present-day mass function and the IMF is $\approx 0.014 M_\odot \text{ pc}^{-3}$ between $1 < M/M_\odot < 3$. If we extrapolate to $M = 8 M_\odot$, this difference is $\approx 0.027 M_\odot \text{ pc}^{-3}$ between $1 < M/M_\odot < 8$. Assuming that all of the stars in this initial mass range turn into white dwarfs, the corresponding mass density of white dwarfs would be $0.0035 M_\odot \text{ pc}^{-3}$ using the initial-mass to final-mass relation of Kalirai et al. (2008), as we will see

below, the mass contained in giant populations is negligible in this context). This is a lower limit, because this estimate does not take into account that the older stars have more extended vertical profiles. Accounting for a typical factor of two difference in z_d between old and young populations, the predicted density of white dwarfs becomes $0.0065 M_\odot \text{ pc}^{-3}$, in good agreement with the value of $0.0056 \pm 0.0010 M_\odot \text{ pc}^{-3}$ from McKee et al. (2015).

When corrected for the effect of vertical heating, we can translate the present-day mass function into a cumulative star formation history. To do this, we integrate the observed number volume density corresponding to the dominant sech^2 component over Z and obtain the observed number surface density for all stellar types. Similar to the volume density above, we can represent the high-mass end as a power law:

$$\frac{dN}{dM} = 9.3 \left(\frac{M}{M_\odot} \right)^{-6.5} M_\odot^{-1} \text{ pc}^{-2}, \quad M > 1 M_\odot. \quad (19)$$

We turn the observed number surface density into an estimate of the total stellar mass formed going backwards in time from the present day up to the main-sequence lifetime of the stellar type, by running an IMF through the surface density measurement of

Table 1. Properties, luminosity function, and mass function of stars along the main sequence.

Spectral type	$J - K_s$	M_V	M_J	Mass M_\odot	n (10^{-4} pc^{-3})	dn/dM_V ($10^{-4} \text{ pc}^{-3} \text{ mag}^{-1}$)	dn/dM ($10^{-4} \text{ pc}^{-3} M_\odot^{-1}$)	$\rho(>M)$ ($10^{-4} M_\odot \text{ pc}^{-3}$)	z_d (pc)
A0V	-0.004	1.34	1.25	2.15	0.38 ± 0.04	1.4 ± 0.2	2.2 ± 0.3	0.8 ± 0.1	49 ± 6
A1V	0.007	1.48	1.32	2.05	0.38 ± 0.04	2.0 ± 0.2	3.0 ± 0.3	1.6 ± 0.2	51 ± 6
A2V	0.024	1.55	1.35	2.00	0.41 ± 0.04	3.9 ± 0.3	5.5 ± 0.5	2.4 ± 0.2	51 ± 6
A3V	0.032	1.76	1.47	1.90	0.69 ± 0.04	4.9 ± 0.3	9.1 ± 0.6	3.7 ± 0.3	46 ± 3
A4V	0.059	1.84	1.51	1.85	0.75 ± 0.05	5.2 ± 0.3	10.1 ± 0.6	5.1 ± 0.4	52 ± 3
A5V	0.069	1.89	1.54	1.83	0.35 ± 0.04	5.4 ± 0.6	10.1 ± 1.1	5.8 ± 0.5	37 ± 6
A6V	0.074	2.07	1.64	1.76	0.60 ± 0.04	5.2 ± 0.4	13.4 ± 0.9	6.8 ± 0.6	53 ± 4
A7V	0.095	2.29	1.78	1.67	1.01 ± 0.05	5.0 ± 0.3	12.6 ± 0.7	8.5 ± 0.6	55 ± 3
A8V	0.117	2.30	1.78	1.67	0.63 ± 0.04	5.5 ± 0.3	14.0 ± 0.8	9.6 ± 0.7	52 ± 4
A9V	0.121	2.51	1.90	1.59	0.65 ± 0.03	5.9 ± 0.3	16.1 ± 0.9	10.6 ± 0.8	56 ± 4
F0V	0.143	2.79	2.13	1.50	1.19 ± 0.06	4.8 ± 0.2	14.0 ± 0.7	12.4 ± 0.8	64 ± 3
F1V	0.166	2.99	2.26	1.44	1.41 ± 0.06	5.9 ± 0.2	18.9 ± 0.8	14.4 ± 0.9	67 ± 3
F2V	0.190	3.08	2.32	1.43	1.23 ± 0.05	8.5 ± 0.4	35.1 ± 1.5	16.2 ± 1.0	64 ± 7
F3V	0.198	3.23	2.42	1.39	0.88 ± 0.04	7.4 ± 0.3	35.3 ± 1.7	17.4 ± 1.1	75 ± 4
F4V	0.211	3.40	2.55	1.33	1.48 ± 0.05	9.3 ± 0.3	29.6 ± 1.1	19.4 ± 1.1	62 ± 7
F5V	0.227	3.70	2.78	1.25	2.54 ± 0.07	10.8 ± 0.3	36.3 ± 1.0	22.5 ± 1.2	80 ± 3
F6V	0.256	3.87	2.90	1.21	3.19 ± 0.08	13.6 ± 0.3	53.2 ± 1.3	26.4 ± 1.3	89 ± 4
F7V	0.273	4.01	3.01	1.18	2.41 ± 0.07	15.5 ± 0.4	68.8 ± 1.9	29.2 ± 1.4	97 ± 5
F8V	0.286	4.15	3.11	1.14	2.54 ± 0.06	18.1 ± 0.5	72.5 ± 1.8	32.1 ± 1.5	104 ± 6
F9V	0.300	4.45	3.34	1.08	4.46 ± 0.09	20.3 ± 0.4	89.3 ± 1.8	36.9 ± 1.6	118 ± 8
G0V	0.329	4.50	3.38	1.07	4.10 ± 0.11	23.4 ± 0.6	117.0 ± 3.1	41.3 ± 1.7	108 ± 11
G1V	0.335	4.79	3.57	1.02	4.21 ± 0.09	24.7 ± 0.5	140.2 ± 3.1	45.6 ± 1.8	177 ± 17
G2V	0.366	4.86	3.64	1.00	4.76 ± 0.12	26.4 ± 0.7	135.9 ± 3.5	50.4 ± 1.9	123 ± 20
G3V	0.373	4.94	3.70	0.99	2.05 ± 0.07	27.4 ± 0.9	136.9 ± 4.6	52.4 ± 2.0	133 ± 39
G4V	0.382	4.98	3.74	0.98	1.49 ± 0.07	24.8 ± 1.1	148.9 ± 6.7	53.9 ± 2.0	–
G5V	0.386	5.13	3.84	0.97	2.51 ± 0.07	26.4 ± 0.8	251.2 ± 7.3	56.3 ± 2.1	–
G6V	0.403	5.18	3.88	0.96	2.59 ± 0.08	25.9 ± 0.8	259.1 ± 7.6	58.8 ± 2.2	–
G7V	0.409	5.32	3.97	0.94	2.39 ± 0.05	25.1 ± 0.5	159.0 ± 3.5	61.0 ± 2.2	–
G8V	0.424	5.55	4.14	0.90	4.67 ± 0.14	25.2 ± 0.8	155.5 ± 4.7	65.2 ± 2.4	–
G9V	0.452	5.76	4.29	0.87	5.22 ± 0.14	23.7 ± 0.6	149.1 ± 4.1	69.8 ± 2.5	–
K0V	0.478	5.91	4.47	0.85	4.01 ± 0.12	22.3 ± 0.7	160.4 ± 4.7	73.2 ± 2.6	–
K1V	0.499	6.19	4.57	0.82	4.65 ± 0.12	21.6 ± 0.6	185.9 ± 4.8	77.0 ± 2.7	–
K2V	0.531	6.57	4.76	0.78	8.89 ± 0.20	26.9 ± 0.6	254.1 ± 5.7	83.9 ± 2.8	–
K3V	0.600	7.04	4.98	0.73	13.72 ± 0.29	32.3 ± 0.7	304.9 ± 6.4	93.9 ± 3.0	–
K4V	0.669	7.25	5.11	0.72	10.87 ± 0.35	32.0 ± 1.0	362.4 ± 11.7	101.8 ± 3.3	–

each stellar type and integrating over all masses. That is, the current surface density $dN_i/dM(\tau_i)$ for a stellar type i with main-sequence lifetime τ_i corresponds to a total stellar mass $\Sigma_*(\tau_i)$ up to τ_i in the past if we anchor an IMF to $dN_i/dM(\tau_i)$ and integrate over all masses. The (reverse) cumulative star formation history of the solar neighbourhood thus determined is displayed in Fig. 15, where the uncertainties are due to the uncertainty in the IMF (marginalizing over the three IMF models that we consider). We see that about $2 M_\odot \text{ pc}^{-2}$ was formed in the last Gyr and that the increase towards higher ages is faster than linear, indicating that the star formation rate has decreased in time.

We fit a model for an exponentially declining (or increasing) star formation rate to these measurements and find that the star formation rate declines in time and is given by

$$\Sigma_{\text{SFR}}(t) = 7.2 \pm 1.0 \exp(-t/7 \pm 1 \text{ Gyr}) M_\odot \text{ pc}^{-2} \text{ Gyr}^{-1}, \quad (20)$$

where t is time measured from 10 Gyr ago. The total amount of stellar mass formed in the last 10 Gyr is $\Sigma_{\text{form}} = 38.5 \pm 2.5 M_\odot \text{ pc}^{-2}$. The declining star formation rate found here is consistent with the analysis of Aumer & Binney (2009), who find the star formation rate to be 2–7 times lower now than at the start of star formation in the disc.

From this measurement of the total mass formed, we can estimate the mass that is presently still contained in visible stars. Based on

maximum masses as a function of age from PARSEC (Bressan et al. 2012) isochrones and a Kroupa (2001) IMF, we find that the ratio of current-to-formed stellar mass is

$$\frac{\Sigma_*(\tau)}{\Sigma_{\text{form}}} = -0.0313 \tau^2 - 0.182 \tau + 0.75, \quad (21)$$

with $\tau = \log_{10}(\tau/\text{Gyr})$ (solar metallicity).

At approximately half-solar metallicity, this fraction is only about a percent lower; for other IMFs (e.g. those from Chabrier 2001), this fraction can be different up to ≈ 5 per cent. For the exponentially declining star formation history, this gives $\Sigma_* = 23.0 \pm 1.5 M_\odot \text{ pc}^{-2}$ or about 60 per cent of the formed mass; this agrees, largely by construction, with directly counting all of the mass above $1 M_\odot$ using equation (19) and combining it with mass below $1 M_\odot$ obtained in a similar manner as for ρ_*^{MS} above: $\Sigma_* = 22.8 \pm 1.0 M_\odot \text{ pc}^{-2}$. For a flat star formation history, the ratio would be ≈ 63 per cent; for a steeply declining star formation history with e -folding time of 1 Gyr, the ratio would be 55 per cent. Considering that we only include stellar mass contained in simple sech^2 components within 400 pc from the mid-plane (what would traditionally be called the ‘thin’ disc), this estimate is in good agreement with previous determinations of the surface density of the thinner component of the disc (Flynn et al. 2006; Bovy, Rix & Hogg 2012a; McKee, Parravano & Hollenbach 2015).

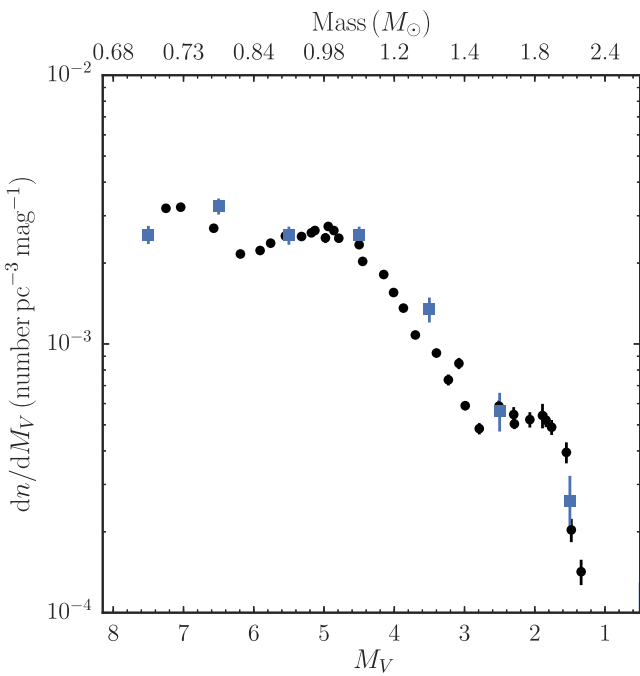


Figure 12. Luminosity function of main-sequence stars from A0V to K5V. Statistical uncertainties are typically smaller than the marker. The blue squares are measurements of the luminosity function from a volume complete sample within 25 pc of the Sun from Reid et al. (2002).

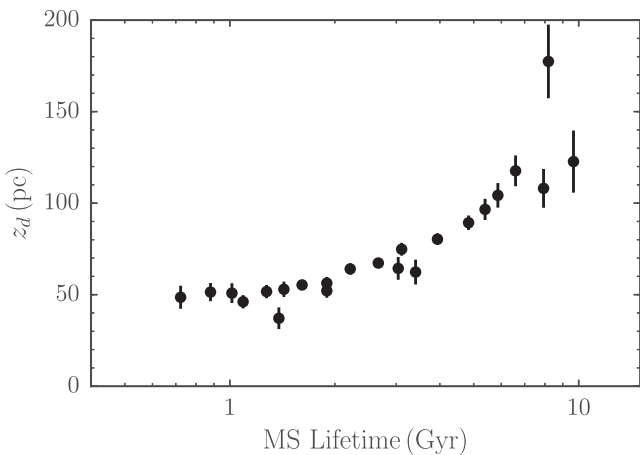


Figure 13. Scaleheight of the sech^2 fits for stellar types along the main sequence (A, F, and early G-type dwarfs to G2V), displayed as a function of their main-sequence lifetime. The scaleheights increase smoothly from ≈ 50 pc for A stars to ≈ 150 pc for early G dwarfs.

Similarly, we determine the ratio of the current mass in white dwarfs versus the total stellar mass formed using the initial–final mass relation from Kalirai et al. (2008) and find that

$$\frac{\Sigma_{\text{WD}}(\tau)}{\Sigma_{\text{form}}} = 0.0222x^2 + 0.0553x + 0.04, \\ \text{with } x = \log_{10}(\tau/\text{Gyr}) \quad (\text{solar metallicity}). \quad (22)$$

At lower metallicity, this ratio is about 0.5 per cent higher. For the exponentially declining star formation history, this gives $\Sigma_{\text{WD}} = 3.6 \pm 0.5 \text{ M}_\odot \text{ pc}^{-2}$ or about 10 per cent of the formed mass (and about 16 per cent of the current stellar mass). For a flat star formation

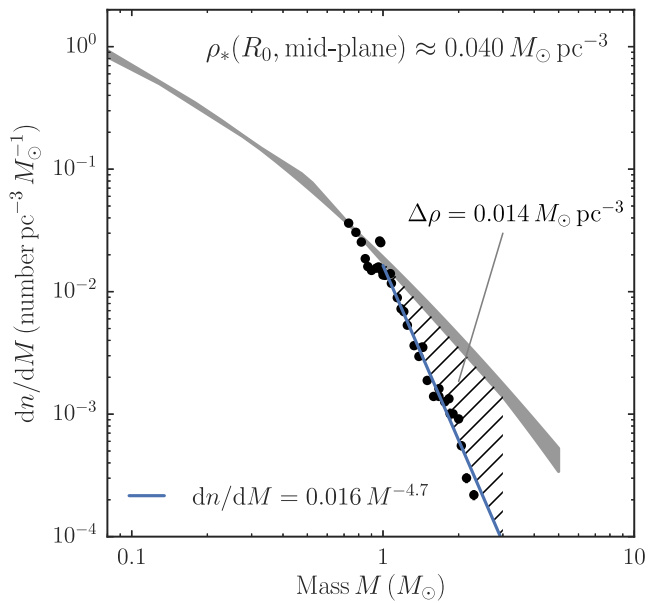


Figure 14. Mass function of main-sequence stars from A0V to K5V. The grey band shows the range spanned by models of the IMF from Chabrier (2001) (lognormal and exponential) and from Kroupa (2001) when anchored to the measured density of long-lived stars ($0.7 \text{ M}_\odot \leq M \leq 0.8 \text{ M}_\odot$). The high-mass end ($M > 1 \text{ M}_\odot$) is fit with the power-law model given by the blue line. Extrapolating below K5V using the IMF model, the total mid-plane stellar density is $0.040 \pm 0.002 \text{ M}_\odot \text{ pc}^{-3}$. Compared to the IMF, the amount of mass in the shaded region is missing due to stellar evolution.

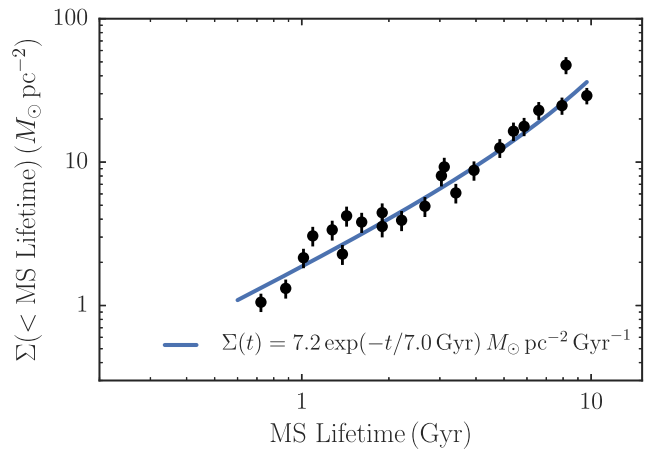


Figure 15. Star formation history of the solar neighbourhood. This figure shows the cumulative total surface density of stars formed as a function of lookback time. These surface densities are obtained by extrapolating the observed column densities of different stellar types to full stellar populations using IMF models under the assumption that each stellar type traces all stars formed up to its main-sequence lifetime. The blue curve is a fit of an exponentially declining star formation rate to these data; uncertainties in the fit parameters are about 15 per cent and almost exactly anticorrelated. The exponentially declining star formation rate provides a good fit to the data. The total amount of mass formed into stars is $38.5 \pm 2.5 \text{ M}_\odot \text{ pc}^{-2}$.

history, the ratio would be ≈ 8.4 per cent (and about 13 per cent of the current stellar mass); for a star-formation history with e -folding time of 1 Gyr, the ratio would be 11.5 per cent (and about 21 per cent of the current stellar mass). Accounting for the about

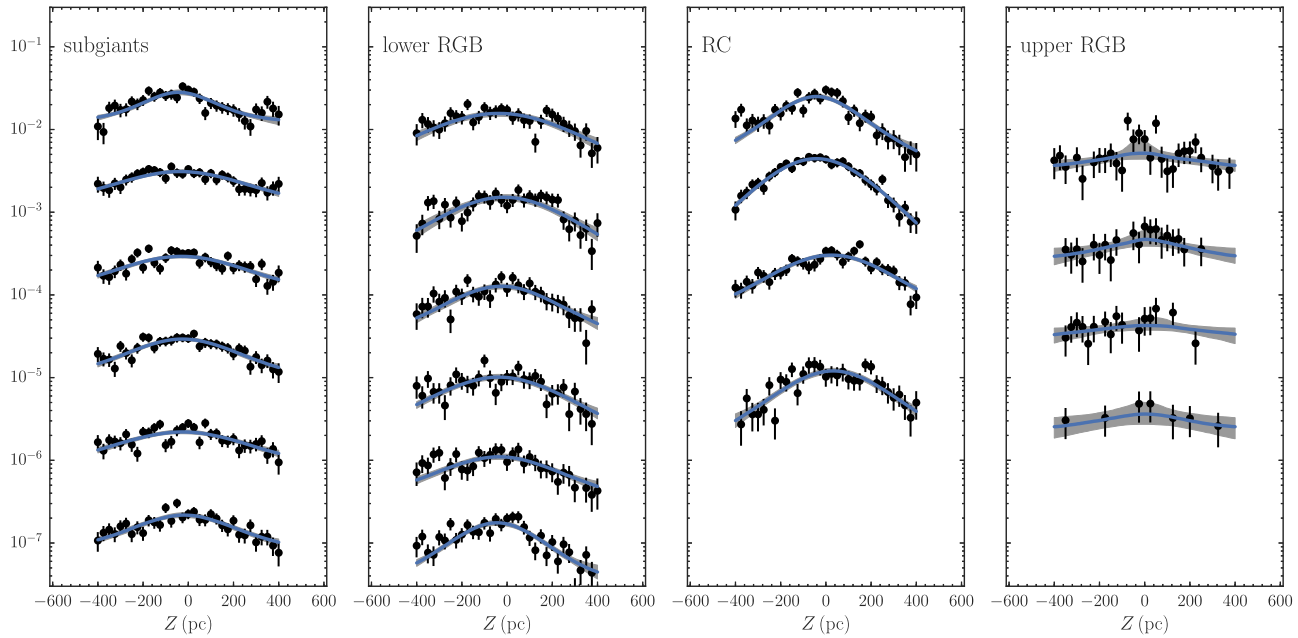


Figure 16. Vertical number density profiles of stars along the giant branch. Giants are separated into $\Delta M_J = 0.25$ mag bins. The black points with uncertainties are the data (TGAS number counts/effective volume), the blue curve is a sech^2 fit, and the grey band is the 68 per cent uncertainty range of the sech^2 model. The profiles have been arbitrarily shifted in the y-direction. As for main-sequence stars, we see that the vertical density clearly flattens near the mid-plane for almost all types of giants.

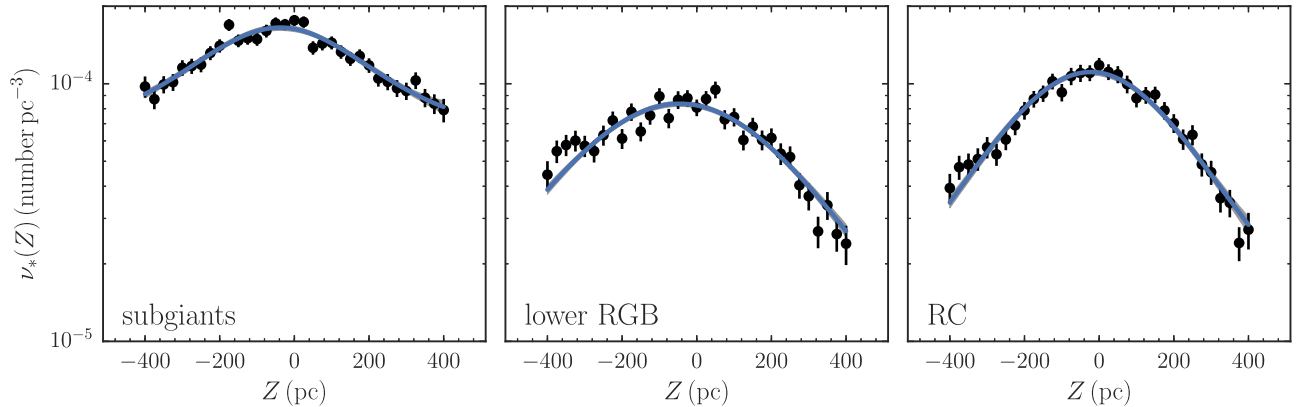


Figure 17. Vertical number density profiles of giants in broad bins in M_J . All stars for a given giant type in Fig. 16 are combined to give a higher quality measurement of their density profiles. The fitted sech^2 profiles have scaleheights of ≈ 150 pc. The Sun's offset from the mid-plane defined by giants is $Z_\odot = 29 \pm 4$ pc, disagreeing with the Sun's offset from the mid-plane defined by A and F stars ($Z_\odot = -0.9 \pm 0.9$ pc; Fig. 19).

$7 M_\odot \text{ pc}^{-2}$ currently in the thicker component of the disc (Bovy et al. 2012a) that we have ignored and that likely has a star formation history more sharply peaked in the past, we estimate a total disc $\Sigma_{\text{WD}} = 5 \pm 1 M_\odot \text{ pc}^{-2}$, again in good agreement with McKee et al.'s (2015) $\Sigma_{\text{WD}} = 4.9 \pm 0.8 M_\odot \text{ pc}^{-2}$.

All in all, the mass distribution of the solar neighbourhood and more broadly the solar cylinder determined from the TGAS star counts is in excellent agreement with previous studies and in many instances substantially more precise.

5 STELLAR DENSITY LAWS FOR GIANT STARS

In the previous section, we discussed the stellar density profiles of different stellar types along the main sequence in detail. We do the same in this section for stars along the giant branch. Similar to the

case of the main sequence above, we count as stars those objects that fall within the lightly shaded region indicated in Fig. 1, including the darkly shaded region. We again ignore dust extinction, because its effect on the effective volume completeness is negligible within the volume that we consider for the purpose of determining vertical density profiles.

5.1 Binned stellar densities along the giant branch

Fig. 16 shows the vertical stellar density profiles for giants in $\Delta M_J = 0.25$ bins, determined from the number counts in a cylinder with a radius of 250 pc in $\Delta Z = 25$ pc bins. Comparing these to each other and to the density profiles of the later stellar types along the main sequence in Fig. 11, we find that these profiles are all very similar. The giant profiles are significantly more noisy than the dwarf profiles, because of the relative paucity of giants in the TGAS

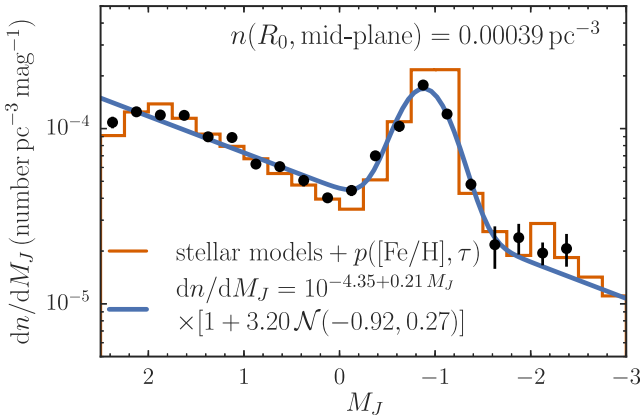


Figure 18. Luminosity function of giants as a function of M_J . Statistical uncertainties are typically smaller than the marker. The luminosity function is well represented by an exponential with a Gaussian RC bump superimposed. The total mid-plane density of giants is $0.00039 \pm 0.00001 \text{ pc}^{-3}$, which corresponds to a total mass density of $0.00046 \pm 0.00005 \text{ M}_\odot \text{ pc}^{-3}$. The orange line shows the prediction from PARSEC stellar models combined with a solar-neighbourhood metallicity distribution and a uniform star-formation history; the overall amplitude of the models is fixed to give our measured total mid-plane density of $0.01 \text{ M}_\odot \text{ pc}^{-3}$ in $M > 0.72 \text{ M}_\odot$ stars and is thus not a free parameter. The agreement between the observed and predicted giant luminosity function in both amplitude and shape is striking.

sample (each $\Delta M_J = 0.25$ bin typically only has about 1000 stars). The measured profiles are well represented by single sech^2 profiles: we find that the amplitude α of a second component when included in the fit is always so small that it is practically insignificant.

To obtain density profiles with smaller uncertainties, we also determine the vertical density of all stars belonging to each major type of giant, because from Fig. 16 it appears that they all have the same vertical profile. This is shown for the subgiants, lower RGB, and RC in Fig. 17; there are too few stars on the upper RGB to obtain a high-precision measurement of the vertical profile. These high-precision profiles demonstrate that the sech^2 fit is indeed a good representation of the giants' density profiles: the profiles clearly display the exponential decline at $|Z| > z_d$ and the flattening near $Z = 0$. The scaleheights of these sech^2 fits are $\approx 150 \text{ pc}$ (subgiants: $130 \pm 20 \text{ pc}$, lower RGB: $100 \pm 33 \text{ pc}$, RC: $154 \pm 10 \text{ pc}$).

5.2 The luminosity function of giants

From the sech^2 fits to the density profiles in Fig. 16, we determine the mid-plane number densities of giants. The luminosity function obtained from these is displayed in Fig. 18 and tabulated in Table 2. This luminosity function has an overall exponential decline towards the upper RGB, with a bump at the location of the RC. The luminosity function is well fit by an exponential function of M_J (or, equivalently, a power law of luminosity), with a Gaussian bump superimposed

$$\frac{dn}{dM_J} = 10^{-4.35+0.21 M_J} \times [1 + 3.20 \mathcal{N}(-0.92, 0.27)], \quad (23)$$

in $\text{number pc}^{-3} \text{ mag}^{-1}$ and where $\mathcal{N}(\mu, \sigma)$ is the (normalized) Gaussian probability distribution with mean μ and standard deviation σ .

The orange curve in Fig. 18 shows the predicted luminosity function from the PARSEC (Bressan et al. 2012) isochrones weighted using a lognormal Chabrier (2001) IMF, a solar-neighbourhood-like

Table 2. Luminosity function of giants.

M_J	n (10^{-4} pc^{-3})	dn/dM_J ($10^{-4} \text{ pc}^{-3} \text{ mag}^{-1}$)	$n(< M_J)$ (10^{-4} pc^{-3})
-2.375	0.05 ± 0.01	0.21 ± 0.05	0.05 ± 0.01
-2.125	0.05 ± 0.01	0.19 ± 0.03	0.10 ± 0.01
-1.875	0.06 ± 0.01	0.24 ± 0.05	0.16 ± 0.02
-1.625	0.05 ± 0.02	0.22 ± 0.07	0.21 ± 0.03
-1.375	0.12 ± 0.01	0.48 ± 0.04	0.33 ± 0.03
-1.125	0.30 ± 0.02	1.21 ± 0.07	0.64 ± 0.03
-0.875	0.44 ± 0.02	1.77 ± 0.07	1.08 ± 0.04
-0.625	0.26 ± 0.02	1.03 ± 0.07	1.34 ± 0.04
-0.375	0.17 ± 0.01	0.70 ± 0.05	1.51 ± 0.04
-0.125	0.11 ± 0.01	0.44 ± 0.03	1.62 ± 0.04
0.125	0.10 ± 0.01	0.40 ± 0.03	1.72 ± 0.04
0.375	0.13 ± 0.01	0.51 ± 0.04	1.85 ± 0.04
0.625	0.15 ± 0.01	0.61 ± 0.05	2.00 ± 0.05
0.875	0.16 ± 0.02	0.63 ± 0.07	2.16 ± 0.05
1.125	0.22 ± 0.01	0.89 ± 0.05	2.38 ± 0.05
1.375	0.22 ± 0.01	0.90 ± 0.04	2.61 ± 0.05
1.625	0.30 ± 0.01	1.19 ± 0.05	2.90 ± 0.05
1.875	0.30 ± 0.01	1.20 ± 0.06	3.20 ± 0.06
2.125	0.31 ± 0.01	1.25 ± 0.06	3.51 ± 0.06
2.375	0.27 ± 0.02	1.09 ± 0.07	3.78 ± 0.06

metallicity distribution function from Casagrande et al. (2011), and a uniform star-formation history, using the same cuts to define the giant branch as used for the data. The amplitude of this predicted luminosity function is set such that the total stellar mass represented by $M > 0.72 \text{ M}_\odot$ stars in the model is $0.01 \text{ M}_\odot \text{ pc}^{-3}$, the total mid-plane density that we directly measured from number counts along the main sequence in Section 4.3 above. The amplitude is thus not fit to the observed luminosity function of giants. It is clear that the agreement between the predicted and the observed luminosity functions for giants is excellent. The overall amplitude, overall decline towards more luminous giants, and the RC bump are all in good agreement.

The total mid-plane density of giants from integrating over the giant luminosity function between $-4 < M_J < 2.5$ is

$$n = 0.00039 \pm 0.00001 \text{ giants pc}^{-3}. \quad (24)$$

Jahreiss & Wielen (1997) find $n = 0.00049 \pm 0.00009 \text{ giants pc}^{-3}$ from a complete sample of giants within 25 pc. This agrees well with the more precise value found here.

To turn this measurement of the mid-plane number density of giants into an estimate of the mid-plane mass density of giants requires the average stellar mass of giants of different luminosities. We determine the stellar mass of giants of a given luminosity M_J using PARSEC (Bressan et al. 2012) isochrones, selecting giants as stars with surface gravities $\log g < 3.75$ and $J - K_s > 0.4$ and marginalizing over a flat star-formation history and the solar-neighbourhood-like metallicity distribution function from Casagrande et al. (2011). The mass function thus obtained is well fit by

$$\frac{d\rho}{dM_J} = 10^{-4.25+0.17 M_J} \times [1 + 2.77 \mathcal{N}(-0.93, 0.28)], \quad (25)$$

in $\text{M}_\odot \text{ pc}^{-3} \text{ mag}^{-1}$. The total mid-plane mass density in giants is $\rho_*^{\text{giants}} = 0.00046 \pm 0.00005 \text{ M}_\odot \text{ pc}^{-3}$, (26)

where the uncertainty is dominated by an (estimated) uncertainty of stellar mass along the giant branch. This is close to the value of $\rho_*^{\text{giants}} = 0.00060 \pm 0.00012 \text{ M}_\odot \text{ pc}^{-2}$ from Flynn et al. (2006).

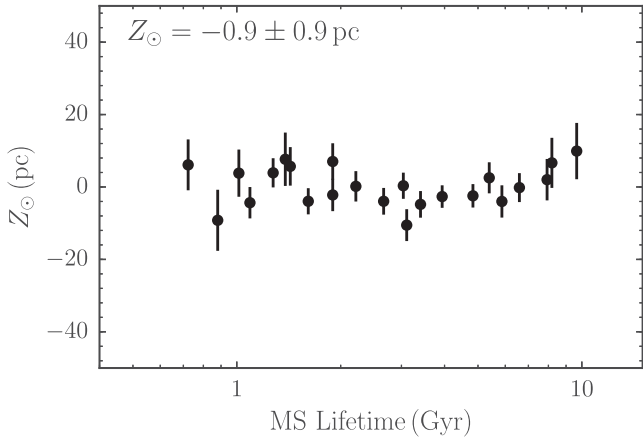


Figure 19. Solar offset from the mid-plane defined by different stellar types. The Sun is consistent with being at the mid-plane defined by A and F dwarfs.

6 THE SUN'S HEIGHT ABOVE THE MID-PLANE

The value of the Sun's offset from the mid-plane defined by each spectral subtype from A0V to G3V is displayed in Fig. 19. For later type dwarfs, we are unable to determine Z_{\odot} , because the stellar density for these stars is almost entirely flat within the observed Z range (see Fig. 11). Remarkably, the Sun is consistent with being at the mid-plane defined by each spectral type, with a combined measurement of $Z_{\odot} = -0.9 \pm 0.9$ pc. For A and F dwarfs, Z_{\odot} is determined from the vertical distribution over ≈ 4 scaleheights in both directions away from the mid-plane, leading to the high precision in the measured Z_{\odot} .

We measure the Sun's offset from the mid-plane defined by the three major, different types of giants (subgiants, lower RGB, and RC) using the density profiles shown in Fig. 17. The measured Z_{\odot} for these three populations are: $Z_{\odot} = 42 \pm 7$ pc (subgiants), $Z_{\odot} > 45$ pc (1σ) (lower RGB), and $Z_{\odot} = 22 \pm 6$ pc (RC). For the lower RGB, we only measure a lower limit with an a priori upper limit of $Z_{\odot} < 50$ pc. This inferred value is strongly affected by the density profile at $|Z| > 200$ pc for lower RGB stars, which is somewhat asymmetric. Only considering lower RGB stars below 200 pc, we find $Z_{\odot} = 25 \pm 13$ pc. Combining this value with the measurements using subgiants and RC stars, we find $Z_{\odot} = 29 \pm 4$ pc with respect to the mid-plane defined by giants. If we only include giants at $|Z| < 200$ pc for all three types, we find $Z_{\odot} = 35 \pm 7$ pc.

We have investigated whether the inferred Z_{\odot} depends on the assumed extinction model. The basic fits shown in Fig. 19 ignore extinction in the calculation of the effective volume completeness, because it has only a minor effect. We have also determined the vertical stellar profiles of entire spectral types – all stars of type AV, all stars of type FV, etc. – taking into account the three-dimensional extinction model discussed in Section 3.2. The inferred Z_{\odot} only differ by ≈ 0.1 pc from those determined without taking extinction into account for A and F dwarfs and by only 1 pc for G dwarfs.

As discussed in Appendix A, our model for the raw TGAS selection function is not perfect at the bright end. This may affect the results derived in this section, especially for the intrinsically bright A and F dwarfs and for red giants, many of which are located near the bright-end cut-off of TGAS. Therefore, we have re-determined the stellar densities, removing all stars with $J_G < 8$ (where J_G is defined in Appendix A), which is where our model for the raw selection function performs poorly. The resulting density profiles are

very similar to those derived from the full data set, although they are much noisier for the earliest A dwarfs. The combined value of the Sun's height above the mid-plane is $Z_{\odot} = -0.3 \pm 1.1$ pc, consistent with the value determined from the full data set. The scaleheight and mid-plane densities are also the same. For giants, we measure $Z_{\odot} = 36 \pm 5$ pc when removing the bright stars and the bright-end behaviour of the TGAS selection can therefore not explain the difference that we find between the Z_{\odot} determined from A/F dwarfs and from giants.

We also investigate whether the wide cylinders (radii of 250 and 200 pc) used to determine the vertical density profiles of A and F dwarfs affect the Solar offset from the mid-plane defined by these populations. We determine the density profiles for all types of main-sequence stars for cylinders with width 150 pc. We find density profiles and sech^2 fits that are almost the same as those based on the wider cylinders for A and F dwarfs. In particular, the Sun's height above the mid-plane defined by A and F dwarfs is $Z_{\odot} = -0.7 \pm 1.3$ pc, fully consistent with the value determined from the wider cylinders.

Finally, we determine the Solar offset only considering density measurements at $|Z| > 100$ pc. We do this because the effective volume completeness for A and F stars has a mildly peaked structure centred on $Z = 0$, due to the bright-end TGAS cut-off and the sky cut (see Fig. 4). If the effective volume completeness is even slightly incorrect, this could induce an apparent peak in the stellar density profile, which is shallow near the plane. At $|Z| > 100$ pc, the effective volume for A and F stars is almost constant with Z . In this case, we find the Sun's height as defined by A and F dwarfs to be $Z_{\odot} = -2.5 \pm 1.2$ pc, consistent with the result from the full data set.

Therefore, the TGAS data strongly prefer a value of Z_{\odot} when measured using A and F dwarfs that is consistent with zero within a few parsecs. However, while we have performed a number of tests, described in the previous paragraphs, of the impact of the TGAS selection function on the measurement of Z_{\odot} , our TGAS selection function is only an empirical model derived using a number of assumptions, including that the selection function does not vary with position on the sky (within the ‘good’ part of the sky). These assumptions are unlikely to be correct in detail and may affect the Z_{\odot} measurement in ways that are not covered by the tests discussed above. The next Gaia DR will not depend on the Tycho-2 catalog and will likely have a simpler selection function than TGAS. This will allow for a more robust determination of Z_{\odot} using various stellar types.

Our results for Z_{\odot} with respect to A/F dwarfs and with respect to giants are at odds with each other. The measured Z_{\odot} with respect to A/F dwarfs also appears to be at odds with previous determinations, which find a canonical value of $Z_{\odot} = 15\text{--}25$ pc (e.g. Binney et al. 1997; Chen et al. 2001; Jurić et al. 2008) and agree with the Solar offset we determine using giants. However, these literature determinations are based on old stellar populations, rather than the young populations traced by A and F stars here. A value of $Z_{\odot} = 25$ pc corresponds to one half of a scaleheight for the A dwarfs and can be clearly ruled out by the TGAS star counts. For younger tracers (young open clusters and OB stars), Z_{\odot} is typically found to be smaller, with $Z_{\odot} = 6\text{--}15$ pc (e.g. Bonatto et al. 2006; Joshi 2007; Joshi et al. 2016), closer to what we determine here. Moreover, measurements of the vertical distribution of atomic (Malhotra 1995) and molecular gas (Nakanishi & Sofue 2006) in the Milky Way find typical fluctuations in the location of their mid-plane of tens of parsecs. These are most likely inherited by newly formed stars and could persist for a few dynamical times for the younger stars traced by A and F dwarfs.

7 DISCUSSION

7.1 Computational complexity

In this paper, we have determined stellar densities using the $N = \mathcal{O}(10^6)$ stars in the *TGAS* catalog. The full *Gaia* data set will eventually consist of $\mathcal{O}(10^9)$ stars and it is therefore urgent to ask how the method used in this paper scales to this much larger number of stars. When determining stellar densities using the formalism in Section 2.2, the main computational complexity arises from the calculation of the effective volume in the denominator in equation (9). The numerator in that expression can be efficiently computed for all volume bins simultaneously (e.g. using a histogram function) using $\mathcal{O}(N)$ operations and is fast even for $\mathcal{O}(10^9)$ stars. The calculation of the effective volume does not scale directly with N , because it does not involve the data, only the selection function. However, because future DRs will cover a larger region of the Galaxy, the numerical integration of the effective volume will extend over a larger area and take longer to compute.

In the limit of vanishing dust extinction, computing the effective volume is easy, because the distance integral can be factored out from the integral on the sky. This is the case as long as the raw selection function does not depend on sky position, except for a purely geometric sky cut, like in our model for the *TGAS* selection function. While the selection function will certainly depend on sky position in small parts of the sky with high stellar density (where *Gaia* cannot catalogue all sources due to telemetry limitations), over most of the sky future *Gaia* selection functions will likely not depend on position on the sky. However, extinction cannot be avoided when determining stellar densities close to the mid-plane and this complicates the effective-volume integral. Figs 4–8 take the full three-dimensional dependence of dust extinction into account and took altogether a few days to compute using dozens of processors. Because the effective volume does not directly scale with the number of data points, as long as the extinction model is kept fixed (or only a small number of alternative models are explored), this computational time will not increase much in future DRs.

7.2 Other uses of the effective completeness for *TGAS*

We have used the effective completeness and the effective volume completeness for *TGAS* from Section 3 only for measuring the vertical density profiles of different stellar types. However, the effective completeness should be taken into account in any use of the *TGAS* data that depends on how the underlying stellar density distribution is catalogued in *TGAS* and this, in principle, includes essentially all use of the *TGAS* parallaxes as distance indicators. Because *Gaia* measures parallaxes rather than distances, any distance inferred from the *TGAS* parallaxes requires a distance prior (Bailer-Jones 2015). This prior should take the effective completeness of *TGAS* into account. For example, to get the best inferred distances using the method of Astraatmadja & Bailer-Jones (2016a), their priors should be multiplied by the effective selection function, which they currently assume is uniform down to a magnitude limit (and they fully ignore the bright cut-off in *TGAS*; Astraatmadja & Bailer-Jones 2016b).

Similarly, because the effective completeness of *TGAS* is a strong function of stellar type (see Fig. 2), any representation of the CMD from *TGAS* data (e.g. in Gaia Collaboration et al. 2016b) has strong selection biases and densities within the colour–magnitude plane do not reflect true, underlying densities, but rather the density of objects

contained in *TGAS*. This has strong implications for any analysis that models the observed CMD and uses it to, for instance, improve distances inferred from the *TGAS* parallaxes without attempting to correct for *TGAS*'s selection biases (e.g. Leistedt & Hogg 2017, Anderson et al. 2017, in preparation). Such models of the CMD cannot be applied to data other than the *TGAS* data themselves, because other data will have a different effective completeness and thus have different biases in the colour–magnitude plane.

More broadly, many analyses of the *TGAS* data that use more than a small volume can be affected by the selection function, even if they do not directly depend on the number counts or underlying stellar densities. For example, analyses of the kinematics – typically assumed to be free of selection biases – of different stellar populations based on *TGAS* may depend on the selection function if they average over large volumes and gradients across this volume are important. For example, suppose one examines the kinematics of stars along the main sequence for a volume with $\sqrt{X^2 + Y^2} < 500$ pc and -100 pc $< Z < 100$ pc. Then, the most luminous main-sequence stars will sample this volume almost uniformly, while the faintest main-sequence stars will only cover the nearest few tens of parsecs and the measured kinematic properties will effectively cover widely different volumes. If Galactic gradients are important, the effective completeness needs to be taken into account when comparing different stellar populations. The completeness maps displayed in Figs 5–8 can act as a guide to determine how important selection effects may be.

7.3 Astrophysical implications

We have obtained a number of new constraints on the stellar-populations structure of the local Milky Way disc from the analysis of the vertical densities of main-sequence and giant stars in *TGAS*. One of the most directly measured quantities is the distribution of stellar mass in the mid-plane along the main sequence covering $0.7 M_{\odot} \lesssim M \lesssim 2.2 M_{\odot}$. While the *TGAS* data represent only a small fraction of the full, final *Gaia* catalog, this range extends both to high enough M such that there is little mass in stellar populations with higher M and to low enough M that we reach the part of the main sequence where stars of any age have not evolved into giants yet. Thus, assuming an IMF model for $M \lesssim 0.7 M_{\odot}$, we obtain a census of all stellar mass in the solar neighbourhood, an important ingredient in the baryonic mass budget in the solar neighbourhood (McKee et al. 2015). Because – beside filling in the $G \lesssim 6$ part of the magnitude distribution and the part of the sky that we have ignored in the selection function – improvements in the sampling of the *Gaia* catalog will primarily come from going to fainter magnitudes and thus larger distances, the census described in this paper is practically the definitive census of $M \gtrsim 1 M_{\odot}$ stars in the solar neighbourhood. However, future DRs will allow the low-mass IMF to be determined from the *Gaia* data and thus improve the census by directly including the contribution of low-mass stars.

We have used the measurements of the intrinsic stellar number counts at $M > 1 M_{\odot}$, after translating them to surface densities to account for vertical heating, to determine the star formation history of the solar neighbourhood. Our measurement in Fig. 15 is a direct measurement of the reverse-cumulative star formation history and thus presents an important new constraint on models for the evolution of the Milky Way disc. However, to make this measurement we had to assume that the slope of the high-mass IMF is constant over the history of the disc and that it is known. Our results are degenerate with the slope of the high-mass IMF. For example, if we assume that the high-mass IMF tracks the

present-day mass function that we measure, the points in Fig. 15 would scatter around a constant value and we would infer that stars only formed during the last few hundred Myr. Using the kinematics of stars along the main sequence in addition to their number densities can help break this degeneracy (Binney et al. 2000) and using the number densities along the giant branch would provide additional constraints (see Fig. 18).

The star formation history that we measure is corrected for vertical heating. However, stars may also heat and migrate in the radial direction (Sellwood & Binney 2002) and the locally measured star formation history in that case is essentially that of annuli in the disc convolved with the migration history (e.g. Schönrich & Binney 2009). If migration is extremely efficient and the disc is fully mixed, the locally measured star formation history would simply be the star formation history of the entire disc. Conversely, if migration is inefficient, the locally measured star formation history reflects the local evolution. The truth most probably lies somewhere in the middle and it is thus difficult to directly relate the locally measured star formation history to the evolution of the solar circle.

7.4 Future work

Future *Gaia* DRs will allow the stellar census performed here to be extended in many ways. Star counts down to $G \approx 20.7$ will allow all stars down to $M = 0.08 M_{\odot}$ to be mapped within ≈ 25 pc and in rapidly increasing volumes for higher masses (e.g. ≈ 190 pc for $M = 0.15 M_{\odot}$, ≈ 500 pc for $M = 0.3 M_{\odot}$). Thus, the completeness maps shown for *TGAS* in Figs 5–8 will cover much larger volumes of the Galaxy beyond the closest kiloparsecs. For all but the faintest stars, the vertical and radial density laws within the Galaxy can be determined to high precision, which will provide an unprecedented view of the distribution of mass and light in a large disc galaxy.

To get the most out of the *Gaia* data, various improvements to the analysis presented in the paper will have to be made. First of all, because no all-sky, complete stellar catalogue currently exists down to $G \approx 20.7$, we will not be able to determine the catalogue completeness by comparing to an external, complete catalogue, as we did for *TGAS* using the 2MASS catalog in Appendix A. Ultimately, the completeness of the *Gaia* catalog should be determined from the *Gaia* data and instrument themselves, by considering how likely it is that sources with a given set of properties (sky location, brightness, colour, etc.) appear in the final catalogue. From the way in which *Gaia* scans the sky it is expected that, but for the most crowded regions of the sky, the final *Gaia* catalog will be 100 per cent complete down to some faint limit. For making the most complete stellar census based on *Gaia* data, determining the completeness around the faint limit will be of great importance, as small magnitude differences at the faint end represent large numbers of stars and large volumes. For example, by determining the completeness of *TGAS* using 2MASS rather than the *Tycho-2* catalog, we were able to extend the magnitude range over which the completeness is understood by ≈ 1.5 mag or a factor of two in distance. For *Gaia* DR2, we can still use 2MASS down to $J \approx 15$ to determine the completeness of the catalogue, an improvement of ≈ 3 mag, or a factor of four in distance, over *TGAS*.

A second necessary improvement concerns the methodology used to infer the underlying stellar density. We have presented the statistical framework for inferring the underlying density from an incomplete survey in Section 2. In the current application of this general methodology, we have assumed that only the underlying stellar density is unknown, while the survey selection function, the density in the CMD ρ_{CMD} , and the three-dimensional extinction map are

presumed to be known. While the survey selection function will hopefully be well known enough from the data processing itself (see previous paragraph), the density in the CMD and the three-dimensional extinction map are far from well known. Determining them is among the other main scientific goals of the *Gaia* mission (Gaia Collaboration et al. 2016a). Because we have focused in this paper on the nearest few hundred parsecs and have used near-infrared photometry, the three-dimensional extinction has only a minor effect on the observed number counts. For the CMD, we were able to approximate the underlying density by focusing on the high-precision parallaxes.

Ultimately, to gain a full, empirical understanding of the stellar distribution, CMD, and three-dimensional extinction throughout the Milky Way, all three should be obtained through a single analysis using the methodology described in Section 2. The likelihood given in the first line of equation (2) is general and could include parameters of flexible models for the CMD and the extinction map (we have only assumed that these are known in the second line of equation 2). So far, studies of the CMD or the three-dimensional extinction map have assumed that the other ingredients are perfectly known. For example, studies of the CMD using *TGAS* data assume that the density distribution and extinction are known (e.g. Leistedt & Hogg 2017, Anderson et al. 2017, in preparation). Similarly, the sophisticated determination of the three-dimensional extinction by Green et al. (2015) assumes that the stellar locus (the CMD) and the density distribution of the Milky Way are known (Green et al. 2014). With more *Gaia* data, especially with the BP/RP photometry, it should be possible to constrain all three ingredients simultaneously.

8 CONCLUSION

We have conducted the first detailed stellar inventory of the solar neighbourhood using the *Gaia* DR1 *TGAS* data. To do this, we have performed a detailed analysis of the raw *TGAS* selection function and have successfully derived the *TGAS* completeness over 48 per cent of the sky with ‘good’ *TGAS* observations. Using this raw completeness, we have determined the effective completeness in distance and volume of different stellar populations in *TGAS*, taking into account their intrinsic distribution in colour and absolute magnitude as well as the three-dimensional dependence of dust extinction. Maps of the completeness of *TGAS* for different stellar tracers are given in Figs 5–8 and these should provide a useful guide for many studies making use of *TGAS* data.

Using our determination of the completeness of *TGAS*, we have measured the intrinsic stellar density distribution for different stellar types along the main sequence and along the giant branch. This results in a detailed new inventory of the stellar mass distribution in the solar neighbourhood given in Tables 1 and 2. We have determined the luminosity function along the main sequence for $7.25 > M_V > 1.34$ (Fig. 12), the present-day mass function for stars with masses $M \gtrsim 0.72 M_{\odot}$ (Fig. 14), and total mid-plane density in stars (equation 18). From these, we have determined the implications for the mass in white dwarfs and we have measured the star formation history of the solar neighbourhood (Fig. 15 and equation 20). We have further determined the luminosity function of stars along the giant branch (Fig. 18) and the total number and mass density of giants in the mid-plane (equations 24 and 26).

We have also measured the vertical density profiles of different types of dwarfs and giants. For all stellar types, we clearly see that the vertical density profiles flatten at $|Z| \lesssim 100$ pc and all profiles are well represented as sech^2 profiles within a few scaleheights ($Z \lesssim 4 z_d$). The scaleheight of these profiles increases smoothly when

going from the earliest A-type dwarfs ($z_d \approx 50$ pc) to late K-type dwarfs ($z_d \approx 150$ pc); giants have similar profiles as late dwarfs. Surprisingly, we find that the Sun is at the mid-plane defined by A-type and F-type dwarfs ($Z_\odot = -0.9 \pm 0.9$ pc), in tension with previous measurements. However, we are unable to identify any systematic in our analysis that would produce this result. With respect to older stars on the main sequence and on the giant branch, we find that the Sun is offset from the mid-plane by $Z_\odot = 29 \pm 4$ pc, in good agreement with previous measurements.

The new stellar inventory made possible by *Gaia* DR1 is in good agreement with previous studies, but substantially more precise for the stars that we directly observe ($M \gtrsim 0.72 M_\odot$). The detailed determination of the completeness of *TGAS* opens up many avenues of investigation using *TGAS* data that depend on how *TGAS* samples the underlying stellar distribution. The methodology for determining the completeness can also be straightforwardly extended three magnitudes fainter for *Gaia* DR2 and the tools developed here will thus remain useful. As described in Appendix A and Section 3, we have made code available that allows the raw and effective selection function for *TGAS* to be evaluated. All of the code used to perform the analysis presented in this paper is available at <https://github.com/jobovy/tgas-completeness>, and can serve as an example of how to use the selection function.

ACKNOWLEDGEMENTS

I thank Dustin Lang for providing the *TGAS*-matched 2MASS data and Chris Flynn and Wilma Trick for helpful comments. JB received support from the Natural Sciences and Engineering Research Council of Canada. JB also received partial support from an Alfred P. Sloan Fellowship and from the Simons Foundation.

This work has made use of data from the ESA mission *Gaia* (<http://www.cosmos.esa.int/gaia>), processed by the *Gaia* Data Processing and Analysis Consortium (DPAC, <http://www.cosmos.esa.int/web/gaia/dpac/consortium>). Funding for the DPAC has been provided by national institutions, in particular the institutions participating in the *Gaia* Multilateral Agreement. This publication makes use of data products from the 2MASS, which is a joint project of the University of Massachusetts and the Infrared Processing and Analysis Center/California Institute of Technology, funded by the National Aeronautics and Space Administration and the National Science Foundation.

Some of the results in this paper have been derived using the HEALPix (Górski et al. 2005), ASTROPY (Astropy Collaboration et al. 2013), and EMCEE (Foreman-Mackey et al. 2013) software packages.

REFERENCES

- Allende Prieto C., Kawata D., Cropper M., 2016, A&A, 596, A98
- Astraatmadja T. L., Bailer-Jones C. A. L., 2016a, ApJ, 832, 137
- Astraatmadja T. L., Bailer-Jones C. A. L., 2016b, ApJ, 833, 119
- Astropy Collaboration et al., 2013, A&A, 558, A33
- Aumer M., Binney J. J., 2009, MNRAS, 397, 1286
- Bahcall J. N., 1986, ARA&A, 24, 577
- Bailer-Jones C. A. L., 2015, PASP, 127, 994
- Binney J., Gerhard O., Spergel D., 1997, MNRAS, 288, 365
- Binney J., Dehnen W., Bertelli G., 2000, MNRAS, 318, 658
- Bok B. J., 1937, The Distribution of the Stars in Space. University of Chicago Press, Chicago
- Bonatto C., Kerber L. O., Bica E., Santiago B. X., 2006, A&A, 446, 121
- Bovy J., 2017, MNRAS, 468, L63
- Bovy J., Rix H.-W., 2013, ApJ, 779, 115
- Bovy J., Rix H.-W., Hogg D. W., 2012a, ApJ, 751, 131

- Bovy J., Rix H.-W., Liu C., Hogg D. W., Beers T. C., Lee Y. S., 2012b, ApJ, 753, 148
- Bovy J., Rix H.-W., Green G. M., Schlafly E. F., Finkbeiner D. P., 2016, ApJ, 818, 130
- Bressan A., Marigo P., Girardi L., Salasnich B., Dal Cero C., Rubele S., Nanni A., 2012, MNRAS, 427, 127
- Buckner A. S. M., Froebrich D., 2014, MNRAS, 444, 290
- Casagrande L., Schönrich R., Asplund M., Cassisi S., Ramírez I., Meléndez J., Bensby T., Feltzing S., 2011, A&A, 530, 138
- Chabrier G., 2001, ApJ, 554, 1274
- Chen B. et al., 2001, ApJ, 553, 184
- Drimmel R., Cabrera-Lavers A., López-Corredoira M., 2003, A&A, 409, 205
- Flynn C., Holmberg J., Portinari L., Fuchs B., Jahreiß H., 2006, MNRAS, 372, 1149
- Foreman-Mackey D., Hogg D. W., Lang D., Goodman J., 2013, PASP, 125, 306
- Gaia Collaboration et al., 2016a, A&A, 595, A1
- Gaia Collaboration et al., 2016b, A&A, 595, A2
- Górski K. M., Hivon E., Banday A. J., Wandelt B. D., Hansen F. K., Reinecke M., Bartelmann M., 2005, ApJ, 622, 759
- Gould A., Bahcall J. N., Flynn C., 1996, ApJ, 465, 759
- Green G. M. et al., 2014, ApJ, 783, 114
- Green G. M. et al., 2015, ApJ, 810, 25
- Høg E. et al., 2000, A&A, 355, 27
- Helmi A., Veljanoski J., Breddels M. A., Tian H., Sales L. V., 2017, A&A, 598, A58
- Holmberg J., Flynn C., 2000, MNRAS, 313, 209
- Hunt J. A. S., Bovy J., Carlberg R. G., 2016, ApJ, 832, L25
- Jahreiss H., Wielen R., 1997, in Perryman M. A. C., Bernacca P. L., eds, ESA SP-402: Hipparcos Venice '97. ESA, Noordwijk, p. 675
- Jahreiss H., Wielen R., Fuchs B., 1998, Acta Hist. Astron., 3, 171
- Joshi Y. C., 2007, MNRAS, 378, 768
- Joshi Y. C., Dambis A. K., Pandey A. K., Joshi S., 2016, A&A, 593, A116
- Jurić M. et al., 2008, ApJ, 673, 864
- Kalirai J. S., Hansen B. M. S., Kelson D. D., Reitzel D. B., Rich R. M., Richer H. B., 2008, ApJ, 676, 594
- Kroupa P., 2001, MNRAS, 322, 231
- Leistedt B., Hogg D. W., 2017, ApJ, preprint (<arXiv:1703.08112>)
- Lindgren L. et al., 2016, A&A, 595, A4
- Malhotra S., 1995, ApJ, 448, 138
- Marshall D. J., Robin A. C., Reylé C., Schultheis M., Picaud S., 2006, A&A, 453, 635
- McKee C. F., Paravano A., Hollenbach D. J., 2015, ApJ, 814, 13
- Nakanishi H., Sofue Y., 2006, PASJ, 58, 847
- Pecaut M. J., Mamajek E. E., 2013, ApJS, 208, 9
- Reed B. C., 2000, AJ, 120, 314
- Reid I. N., Gizis J. E., Hawley S. L., 2002, AJ, 124, 2721
- Scalo J. M., 1986, Fundam. Cosm. Phys., 11, 1
- Schönrich R., Binney J., 2009, MNRAS, 396, 203
- Sellwood J. A., Binney J. J., 2002, MNRAS, 336, 785
- Skrutskie M. F. et al., 2006, AJ, 131, 1163

APPENDIX A: THE COMPLETENESS OF TGAS IN COLOUR–MAGNITUDE SKY POSITION

Gaia DR1 consists of two astrometric solutions (Gaia Collaboration et al. 2016b; Lindegren et al. 2016): the primary *TGAS* data set containing positions, parallaxes, and proper motions for a subset of the *Tycho-2* catalog (Høg et al. 2000) and the secondary data set with approximate positions for stars brighter than $G \approx 20.7$. The primary solution consists of 2057 050 stars out of 2539 913 stars in *Tycho-2*. The *Tycho-2* catalog is 99 per cent complete down to $V \approx 11$ and its completeness drops quickly at fainter magnitudes. However, *TGAS* does not share this simple completeness limit, as many of the ≈ 20 per cent of missing stars are at much brighter magnitudes and the very brightest stars ($G \lesssim 6$) are missing, because the specialized

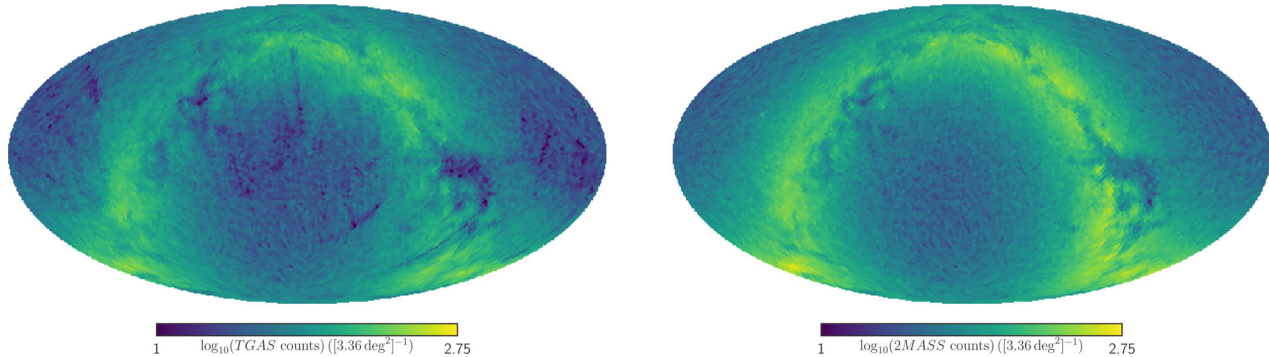


Figure A1. *TGAS* and *2MASS* number counts for stars with $0 < J - K_s < 0.8$ and $6 < J < 10$. While *2MASS* is complete in this range, *TGAS* has artefacts that are mainly due to its scanning pattern. We define the overall completeness in 3.36 deg^2 HEALPix pixels ($N_{\text{side}} = 2^5$) in the following figures to be the ratio of these *TGAS* counts to the *2MASS* counts.

observing mode that they require is not yet sufficiently calibrated to produce reliable results. Due to the inhomogeneity of the scanning law, the completeness also strongly varies over the sky. In this appendix, we investigate the completeness of *TGAS*.

A1 Overall completeness

Almost all of the *Tycho-2* stars were considered in the primary astrometric solution and the main reasons that stars failed to be included in *TGAS* are: (i) they are too bright ($G \lesssim 6$) or (ii) the quality of their astrometric solution is too low (as evidenced by a parallax uncertainty larger than 1 mas or a position uncertainty larger than 20 mas; Lindegren et al. 2016). While the hope is that the astrometric uncertainties will eventually be dominated by photon noise and, therefore, apparent magnitude, the quality of the astrometry in *Gaia* DR1 is primarily set by observational limitations and systematic uncertainties: the lack of high numbers of observations in certain parts of the sky, limitations in the current attitude model, and the simplistic modelling of the point-spread function. The completeness is therefore also in large part a function of broad observational properties (such as the number of astrometric transits) and colour, but to a lesser degree of apparent magnitude (above the faint limit of *Tycho-2*).

Because the data processing for the secondary solution, which contains sky positions and broad-band G magnitudes down to $G \approx 20.7$, is still in a preliminary state, we cannot assume that the secondary solution is a complete sample that we can use to assess the completeness of *TGAS*. We could use *Tycho-2* as the reference catalogue, but this would limit any use of the *TGAS* selection function to $V \lesssim 11$, the 99 per cent completeness limit of *Tycho-2* (without modelling the completeness of *Tycho-2* itself). As we will see below, *TGAS* is 50 per cent complete in at least half of the sky down to $V \approx 12$ and about 20 per cent complete down to $V \approx 12.5$, allowing us to extend *TGAS* coverage about a factor of two in distance and eight in volume beyond the nominal *Tycho-2* limit.

We therefore use the *2MASS* (Skrutskie et al. 2006) Point Source Catalog, which is >99 per cent complete down to $J = 15.8$ and $K = 14.3$ over almost the entire sky. As we will see below, this is at least two magnitudes fainter than the *TGAS* completeness limit even in the best parts of the sky and therefore suffices for our purposes. We select unique (`use_src = '1'`), reliable point sources in *2MASS* that either have signal-to-noise ratio greater than 10 in J (`ph_qual = 'A'`) or are brighter than the detector saturation limit in either the ‘Read 2 – Read 1’ or in the ‘Read 1’ exposures and similarly in K_s .

We assess the overall completeness by comparing the number of point sources with $6 < J < 10$ and $0 < J - K_s < 0.8$ in *TGAS* and *2MASS*. The number counts on the sky in the two catalogues are shown in Fig. A1. Here and in what follows, we bin the sky using HEALPix² level $N_{\text{side}} = 2^5 = 32$. At this level, the sky is divided into 12 288 equal-area pixels that have an approximate size of $1^\circ 8$ and an approximate area of 3.36 deg^2 . This size was chosen as a compromise between large pixels for good Poisson statistics on number counts in *TGAS* and *2MASS* and small pixels that resolve the small-scale structure in the *Gaia* DR1 scanning law. These pixels are small enough to clearly display the structure in the scanning law (see Fig. A2 below). By comparing the *2MASS* counts to the *TGAS* counts in this relatively bright magnitude range, it is clear that while overall the counts are similar, the *TGAS* counts have significant features that are absent in *2MASS*.

We extract some of the main properties of the *Gaia* DR1 scanning law and data processing directly from the *TGAS* catalogue. Fig. A2 displays the mean number of astrometric transits, the spread in this number, the mean spread in the scan directions (the direction along which stars transit the CCDs, using the catalogue entry `scan_direction_strength_k4`), and the mean parallax uncertainty as a function of position on the sky. The mean number of observations clearly shows the imprint of the scanning law, with very few transits near the ecliptic, many near the ecliptic poles, and narrow ridges of abundant transits in ellipsoidal regions around the ecliptic. The spread in the number of transits is small, except in the ellipsoidal regions, which in reality are narrower than our pixel size. Below, we will remove the small part of the sky with high spread in the number of observations, because our sky pixelization is inadequate there. Over the majority of the sky our pixelization captures the properties of the observations well.

The lower left panel in Fig. A2 displays a measure of how well distributed the scan directions are in different parts of the sky. Because *Gaia* essentially performs one-dimensional scans, the astrometric accuracy is higher when different transits scan through a given field at a large variety of angles. As expected, the spread in fields near the ecliptic is small, because these fields have had few transits and thus cannot have a large spread in scan directions. However, the regions near the ecliptic poles also have a relatively small spread in scan directions, even though they have had many observations. As is clear from the lower right panel with the mean parallax

² See <http://healpix.sourceforge.net>.

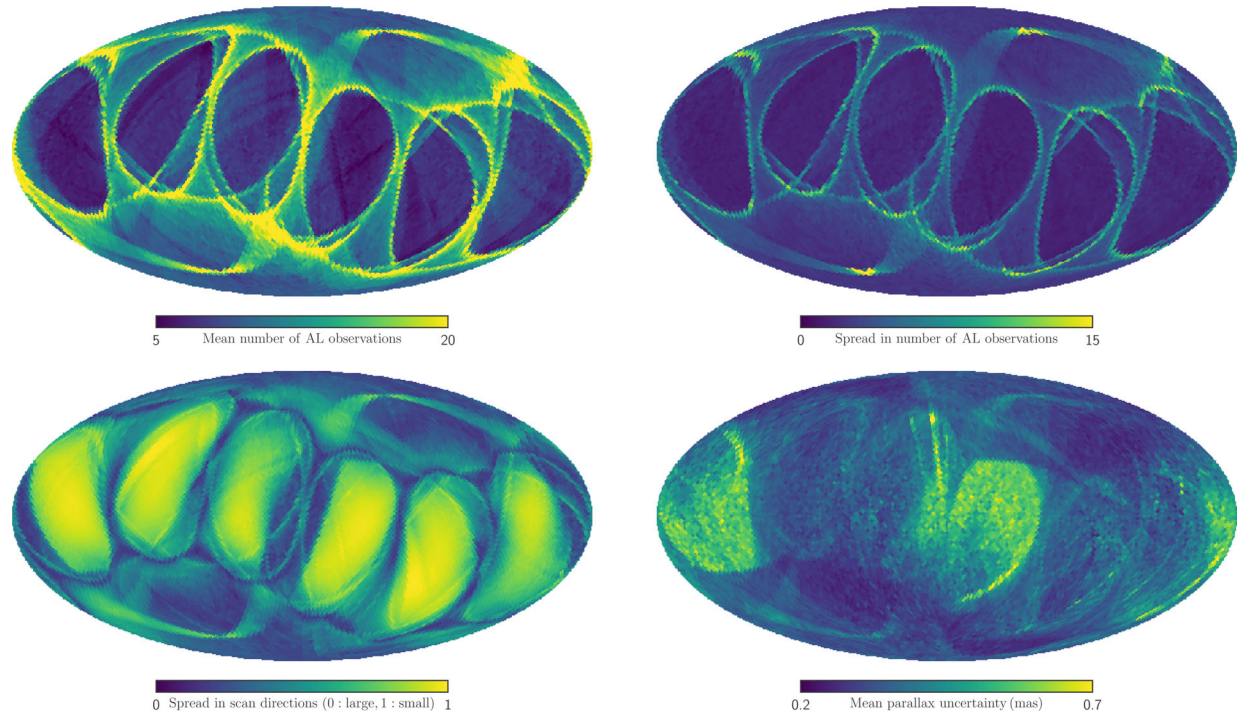


Figure A2. Properties of the TGAS scanning law and catalogue relevant for the determination of the TGAS selection function. The panels show the following in 3.36 deg^2 ($N_{\text{side}} = 2^5$) HEALPix pixels: (a) the mean number of along-scan (AL) observations (divided by nine to account for the nine astrometric CCDs, such that one observation corresponds to one focal-plane crossing) [top left], (b) the standard deviation of the number of AL observations [top right], (c) the spread in the scan directions of different transits (as traced by `scan_direction_strength_k4`; a small value indicates a large spread in the scan directions, which improves the astrometric solution) [bottom left], and (d) the mean parallax uncertainty [bottom right]. Due to the short period of observations covered by Gaia DR1, a large area around the ecliptic currently has a small number of transits, with accordingly a small spread in the scan directions necessary for good astrometry. Areas with high numbers of transits are so narrow that the spread in the number of transits even in 3.36 deg^2 pixels is large and the astrometric quality likely also varies strongly within these pixels. These effects lead to an increase in the typical parallax uncertainty and to decreased completeness.

uncertainty, the regions near the ecliptic have relatively large astrometric uncertainties because of this small spread in scan directions.

Comparing Figs A1 and A2, one can see that many of the artefacts in Fig. A1 are aligned with features in the scanning law. In many cases, these features coincide with the narrow ridges of the ellipsoidal rings around the ecliptic, which have large numbers of transits and one would, thus, naively expect to have high completeness.

We compute the overall completeness as the ratio of the TGAS counts in the range $6 < J < 10$ and $0 < J - K_s < 0.8$ to those in 2MASS. These ranges were chosen to contain enough stars in TGAS to allow a precise measurement (that is, not too hobbled by Poisson noise) of the completeness as a function of position on the sky using the above pixelization. The overall completeness is shown as a function of the properties of the scanning law and of the mean J and $J - K_s$ colour in Fig. A3. It is clear that a low number of transits is most strongly associated with low overall completeness (top-left panel). The overall completeness quickly drops for regions with less than 10 transits. The overall completeness is also low when the spread in the scan directions is small (top-right panel). As discussed above, some of the fields with a large number of transits, but also a large spread in the number of transits have low completeness.

Based on these considerations of the Gaia DR1 scanning law, we define a ‘good’, or well observed, part of the sky as those pixels that satisfy the following cuts:

- (i) Mean number of AL observations ≥ 8.5 ;
- (ii) Spread in number of AL observations ≤ 10 ;
- (iii) Spread in scan directions ≤ 0.7 ;

(iv) $|\text{Ecliptic latitude}| \geq 20^\circ$.

The last cut serves only to remove about 11 per cent of the sky that would otherwise remain as small, isolated islands around the ecliptic. These cuts select 48 per cent of the sky. Of the remaining 52 per cent, 7 per cent is removed because it has a low number of transits (but otherwise good observations), 5 per cent because it has a small spread in scan directions, and 28 per cent because it has both a low number of transits and a small spread in scan directions. About 1 per cent of the sky is excluded because it has a large spread in the number of transits (the ellipsoidal ridges in Fig. A2).

The overall completeness in the ‘good’ part of the sky is displayed in Fig. A4. It is clear that the overall completeness is largely isotropic and does not contain sharp features. The overall completeness is slightly lower near the Galactic plane (which runs through much of the light-green parts of this map), which is because the mean J is somewhat fainter near the plane and TGAS is not complete down to $J = 10$ at all colours (see below). The sky pixels selected by the above cuts are shown as blue dots in Fig. A3. The cut to the ‘good’ part of the sky selects regions that by and large have the same colour and apparent magnitude distribution as the rest of the sky. The mean parallax uncertainty in the ‘good’ part of the sky is typically $\sigma_\pi < 0.45 \text{ mas}$.

A2 Completeness as a function of colour and magnitude

The overall completeness in the ‘good’ part of the sky selected in the previous subsection does not appear to have any significant residual dependence on position on the sky (see Fig. A3). Therefore, we

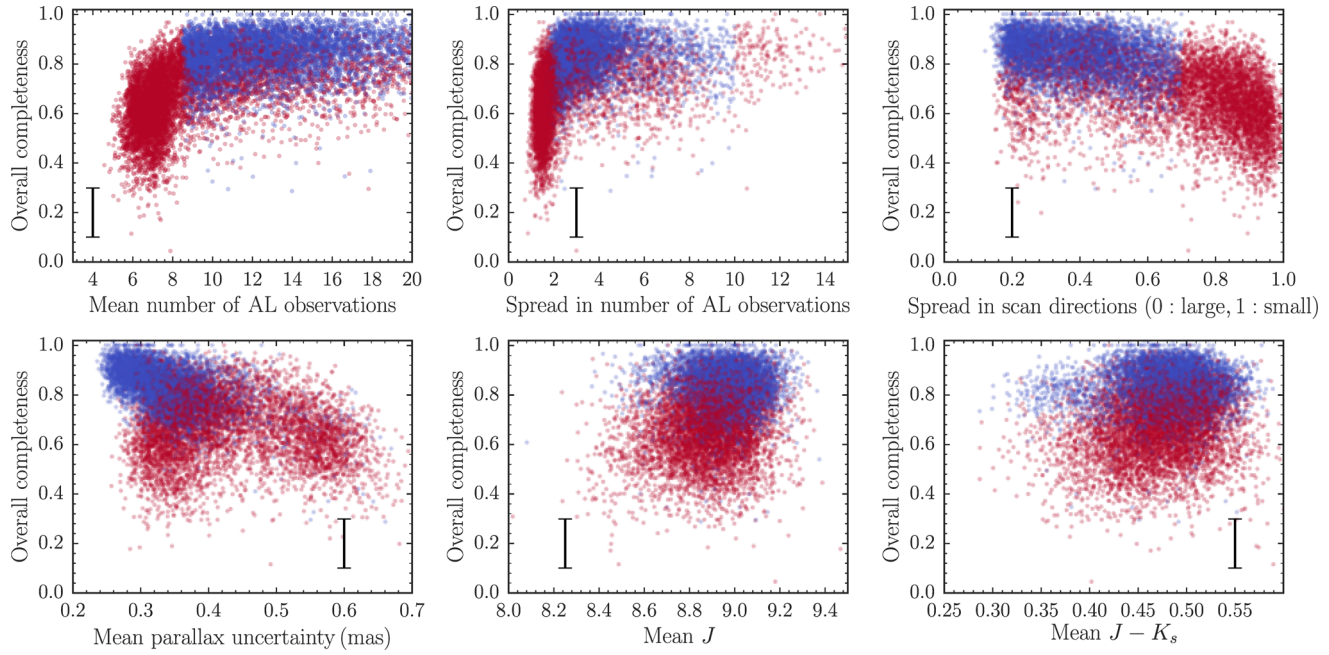


Figure A3. Overall completeness in 3.36 deg^2 sky pixels as a function of properties of the observations in these pixels (see Fig. A2; additionally we display the mean J -band magnitude and the mean $J - K_s$ colour). The error bar gives the typical uncertainty in the completeness. Low numbers of transits or a small spread in the scan directions are associated with a lower overall completeness. The blue points are sky locations that satisfy our TGAS observational quality cuts that select regions of high completeness, the red points cover the remaining part of the sky. The typical magnitude and colour of the locations satisfying our quality cuts are similar to those of the rest of the sky.

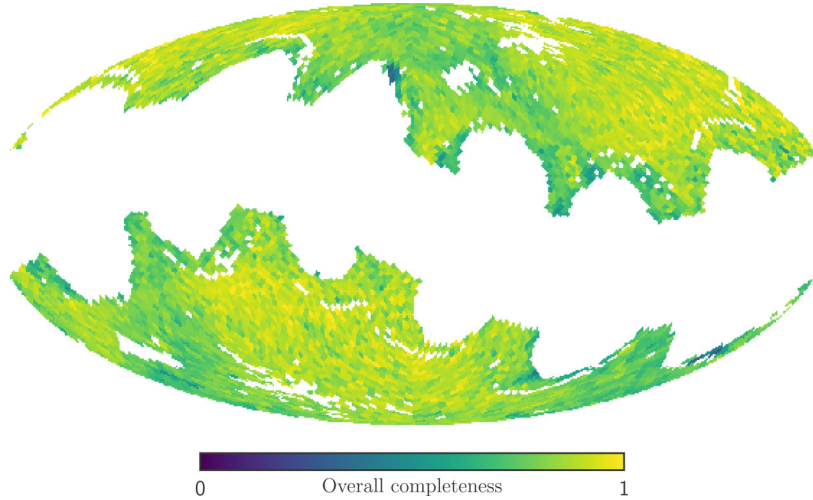


Figure A4. Overall completeness in the ≈ 48 per cent of the sky that satisfies our TGAS observational quality cuts. The overall completeness in this part of the sky is largely isotropic. The Galactic plane has slightly lower overall completeness, because its magnitude distribution is skewed towards fainter magnitudes where it is affected by the incompleteness of TGAS.

continue under the assumption that the completeness in the ‘good’ region of the sky does not depend on sky position. We can then use the large number of stars in this region of the sky to determine the dependence of the TGAS completeness on colour and magnitude in detail.

Fig. A5 displays number counts in TGAS and 2MASS in the ‘good’ part of the TGAS sky in the range $-0.05 < J - K_s < 1$ and $J < 14$ as a function of $(J - K_s, J)$. The main features of the distribution at brighter magnitudes are the same in both catalogues, but there is both a lack of stars in TGAS at the bright and faint ends. At the faint end in particular, there is a steep cut-off in the TGAS number counts that is absent in 2MASS and there-

fore needs to be because of the TGAS selection. This cut-off has a strong dependence on colour, the approximate shape of which is indicated by the dashed line. The overall number counts (summed over $J - K_s$ in the $-0.05 < J - K_s < 1$ range) are shown in Fig. A6. These number counts demonstrate the same bright- and faint-end cut-offs. The faint-end cut-off appears broad in this representation because it is summed over colour. It is also clear that the TGAS counts nowhere quite reach the 2MASS counts, they fall short at every magnitude.

The TGAS completeness computed as the number counts in TGAS divided by those in 2MASS is displayed in Fig. A9. This clearly shows the sharp drop in the completeness at faint magnitudes. To

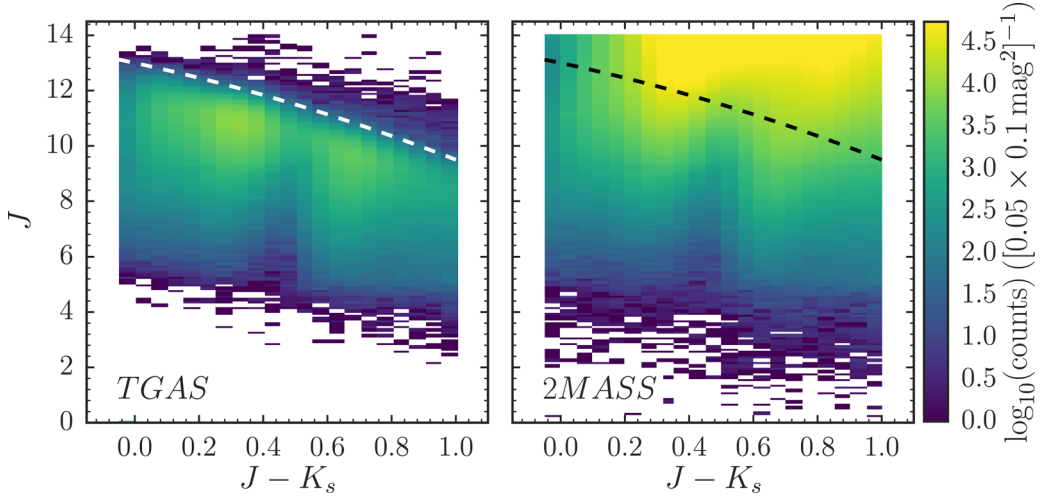


Figure A5. Number counts as a function of $(J, J - K_s)$ for TGAS and 2MASS in the ‘good’ 48 percent of the sky. The dashed line ($J = 13 - (J - K_s)^2 - 2.5(J - K_s)$) indicates the location of a sharp drop-off in the TGAS number counts that is not present in 2MASS and is therefore due to the TGAS selection. In $(J, J - K_s)$, the TGAS selection function depends on colour.

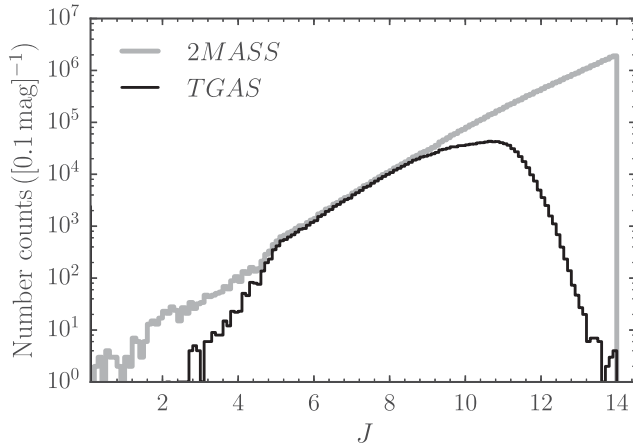


Figure A6. Number counts as a function of J for TGAS and 2MASS in the ‘good’ 48 percent of the sky. TGAS is incomplete at both the bright and faint end with broad drop-offs. This broadness is due to the colour-dependence of the selection function in Fig. A5, which smears out the sharper cut in the two-dimensional $(J, J - K_s)$ plane.

remove the strong colour dependence of the completeness cut-off, we adjust the J magnitude to a new $J_G = J + (J - K_s)^2 + 2.5(J - K_s)$ that runs approximately parallel to the completeness cut-off. This line for $J_G = 12$ is shown in Fig. A9. The $J - K_s$ colour dependence is essentially caused by our use of a near-infrared colour and magnitude for a survey whose completeness is more appropriately a function of an optical magnitude. The $J \rightarrow J_G$ relation is close to the relation that maps $J \rightarrow G$ along the stellar locus.

The number counts in TGAS and 2MASS as a function of J_G are shown in Fig. A7; the TGAS number counts drop more steeply in J_G than they do in J . The completeness (ratio of TGAS to 2MASS number counts) as a function of $(J - K_s, J_G)$ is displayed in Fig. A8. It is clear that the definition of J_G has succeeded in removing the colour dependence of the faint-end cut-off. A slight colour dependence in both the level of the completeness around $J_G = 10$ and in the bright cut-off remains. We ignore the latter, because for star counts there are very few stars at these bright magnitudes that con-

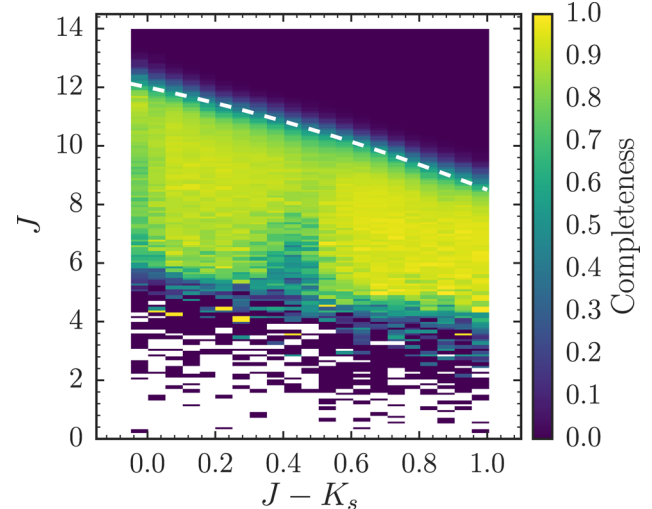


Figure A7. TGAS completeness with respect to 2MASS as a function of $(J, J - K_s)$. This is the ratio of the left- and right-hand panels of Fig. A5. The dashed line is one magnitude brighter than in Fig. A5: $J = 12 - (J - K_s)^2 - 2.5(J - K_s)$. This is the approximate magnitude to which TGAS is 50 per cent complete at the faint end.

tribute to the stellar density. To deal with the former, we divide the colour range in three equal-sized bins with $\Delta J - K_s = 0.35$ in the range $-0.05 < J - K_s < 1$ and approximate the selection function as being a function of J_G only within each bin. The completeness in these bins as a function of J_G is shown in Fig. A10 (for easier interpretability, we have translated J_G to J at the centre of each bin). The grey curve is a smooth spline fit.

The final model for the TGAS selection function $S(J, J - K_s, \alpha, \delta)$ is therefore the function that is (i) zero for (α, δ) outside of the ‘good’ part of the sky and (ii) given by the smooth spline model for the colour bin in which $J - K_s$ is located, evaluated at J_G . We do not model stars bluer than $J - K_s = -0.05$ (mainly O and B stars) or redder than $J - K_s = 1$. This model for the raw TGAS selection function is available in the `gaia_tools.select.tgasSelect`

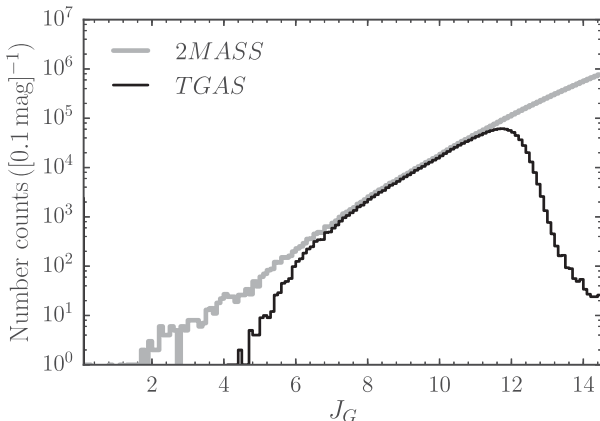


Figure A8. Number counts as a function of $J_G = J + (J - K_s)^2 + 2.5(J - K_s)$ for TGAS and 2MASS in the ‘good’ 48 per cent of the sky. The completeness of TGAS is approximately independent of colour in J_G : TGAS drops off more sharply than in Fig. A6.

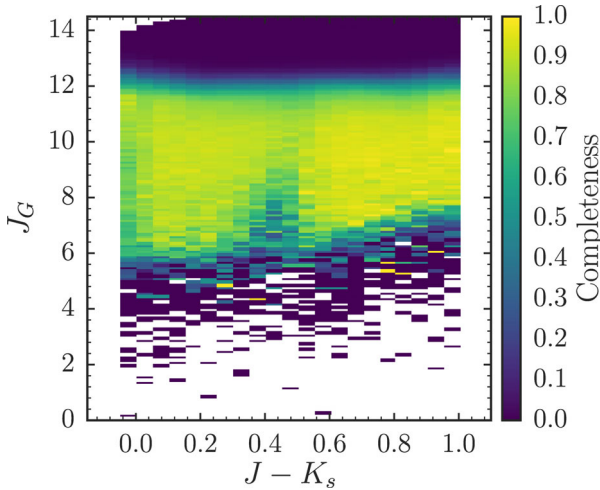


Figure A9. TGAS completeness with respect to 2MASS as a function of $(J_G, J - K_s)$. The completeness of TGAS is approximately independent of colour in J_G . The completeness at redder ($J - K_s$) is slightly higher than at the blue end and we determine the selection function in three broad ($J - K_s$) bins to account for this.

class in the `gaia_tools` package available at https://github.com/jobovy/gaia_tools.

A3 Comparison with Tycho-2

We test our model for the TGAS selection function by determining the completeness of TGAS with respect to its parent catalogue *Tycho-2* at apparent magnitudes brighter than the 99 per cent completeness limit of *Tycho-2* ($V \approx 11$). Similar to how we determine the TGAS selection function above by comparing TGAS number counts to number counts in 2MASS, we compute the number counts as a function of colour $B_T - V_T$ and magnitude V_T in the ‘good’ part of the sky (where our model for the selection function is applicable). These number counts for TGAS and *Tycho-2* are displayed in Fig. A11. The ratio of these number counts gives the completeness of TGAS with respect to *Tycho-2* and this ratio is shown in the left-hand panel of Fig. A12.

Our model for the TGAS selection function is a function of $(J, J - K_s)$ and to compare it to the *Tycho-2* number counts we need to translate the model to $(V_T, B_T - V_T)$. We do this using the following colour-colour transformations

$$J - K_s = 0.55(B_T - V_T) - 0.02, \quad (\text{A1})$$

$$V_T - J = -0.21(B_T - V_T)^2 + 1.8(B_T - V_T) + 0.1. \quad (\text{A2})$$

Evaluating our model for the selection function as a function of $(V_T, B_T - V_T)$ using these relations, we obtain the model displayed in the right-hand panel of Fig. A12. Because we use deterministic colour-colour relations that do not account for the scatter in this transformation, our model evaluated as a function of $B_T - V_T$ is constant in three $B_T - V_T$ ranges (owing to the fact that this is true for the model as a function of $J - K_s$). Comparing the measured TGAS/*Tycho-2* completeness to the model in Fig. A12, we find that the overall agreement of our model with the measurement is good. The model captures the shape and amplitude of the completeness from the bright end to the faint end and from the blue end to the red end.

A more detailed comparison is shown in Fig. A13. This figure compares the completeness as a function of V_T of TGAS versus *Tycho-2* derived from the TGAS and *Tycho-2* number counts to the model in eight bins in $B_T - V_T$. The model agrees well with the data in almost all cases, except (i) at the bright end in almost all

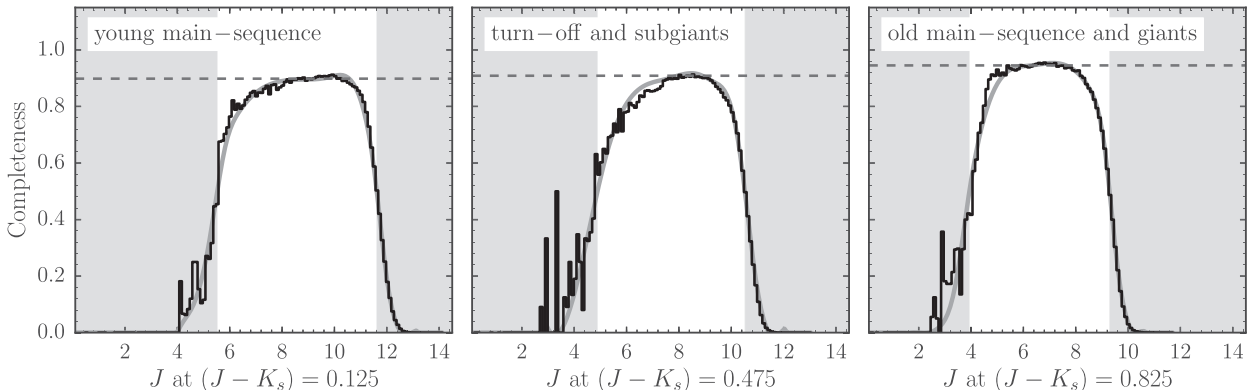


Figure A10. TGAS completeness in the three broad ($J - K_s$) bins in which we determine it ($\Delta J - K_s = 0.35$ over $-0.05 < J - K_s < 1$). Natively, the completeness is a function of J_G ; we have translated this to J for the central colour of each bin. The dashed line indicates the approximate plateau at intermediate magnitudes and the area between the grey bands is where the completeness is higher than 50 per cent. The thick grey curve is a smooth interpolation of the histogram that we use as our model for the selection function.

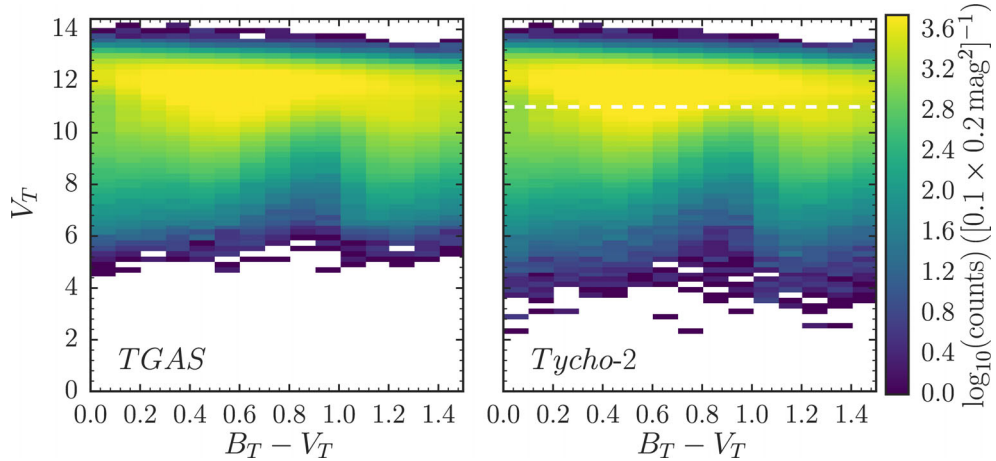


Figure A11. Number counts as a function of (V_T , $B_T - V_T$) for *TGAS* and *Tycho-2* in the ‘good’ 48 per cent of the sky. The dashed line at $V_T = 11$ indicates the location of the 99 per cent completeness limit of *Tycho-2*. *TGAS* closely traces its parent catalogue *Tycho-2*.

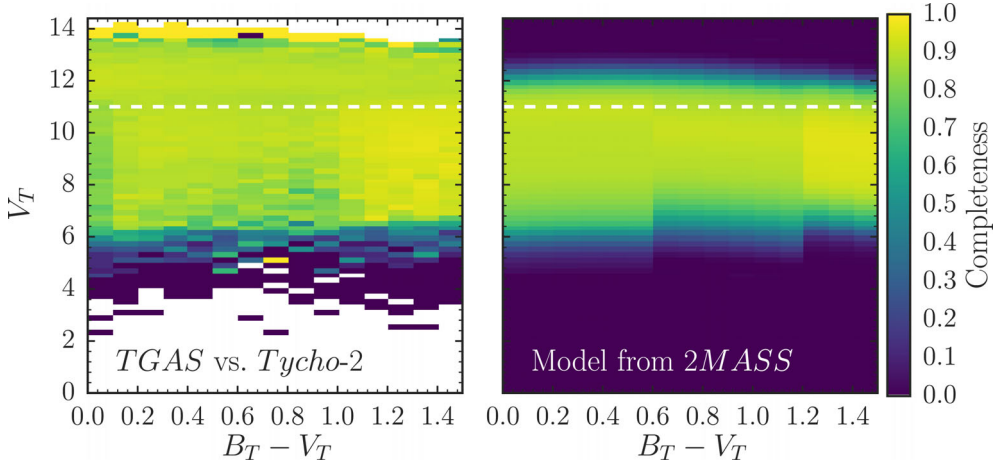


Figure A12. *TGAS* completeness with respect to *Tycho-2* as a function of (V_T , $B_T - V_T$) (left-hand panel). This is the ratio of the left- and right-hand panels of Fig. A11. The right-hand panel represents our model for this completeness derived from (a) the *TGAS* selection function derived from comparing *TGAS* to 2MASS and (b) colour-colour transformations between the visible and near-infrared photometric bands (because we do not include scatter in the colour transformations, the completeness is constant within three colour bins as it is in the model). The dashed line in both panels is the 99 per cent completeness limit of *Tycho-2*. Overall, our model for the selection function matches the amplitude and the lower and upper cut-offs in the completeness.

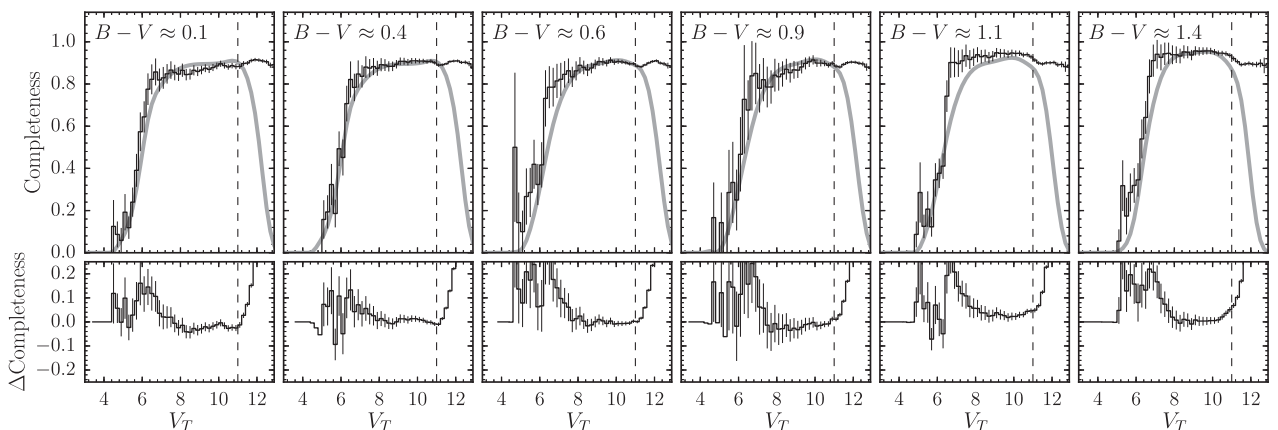


Figure A13. Comparison between the completeness of *TGAS* with respect to *Tycho-2* in six $B_T - V_T$ colour bins measured directly by comparing *TGAS* and *Tycho-2* number counts (histogram with uncertainties) and derived from our model for the *TGAS* selection function (smooth, grey curve). The top panel directly compares the two, the bottom panel displays the residual (direct minus model). The dashed line is the 99 per cent completeness limit of *Tycho-2*, beyond which the direct measurement is meaningless. Overall the model represents the completeness well, with some (expected) deviations at the bright end and around $B - V \approx 1.1$.

colour bins and (ii) in its overall amplitude around $B_T - V_T \approx 1.1$. These discrepancies are expected based on how we determined the selection function above. To produce a simple model that accurately describes the faint end of the completeness, we performed a simple transformation $(J, J - K_s) \rightarrow J_G$ in which the faint-end cut-off is independent of colour. However, the completeness at the bright end does depend on colour in J_G and our model does not capture this dependence. This causes the discrepancy at the bright end of the completeness in $(V_T, B_T - V_T)$. Clearly, the completeness has a simpler colour dependency in $B_T - V_T$ than in $J - K_s$, so if we had a complete optical survey we could determine a more accurate selection function. For the purpose of this paper, a small discrepancy at bright magnitudes does not influence our results much, because very few stars have such bright magnitudes.

The discrepancy near $B_T - V_T \approx 1.1$ is caused by our choice of binning in $J - K_s$. For ease of interfacing with the large 2MASS data base, the $J - K_s$ colour bins were chosen to be equal size and our binning does not perfectly capture the higher completeness at

the red end. This shows up most prominently around $J - K_s \approx 0.6$ or $B_T - V_T \approx 1.1$, which falls in the middle colour bin of the model, but in reality is closer to the higher completeness of the reddest colour bin of the model. The discrepancy amounts to only a few per cent underestimation of the completeness in a narrow colour strip.

APPENDIX B: OVERALL COMPLETENESS OF THE LOW-QUALITY PORTION OF THE SKY

We present the overall completeness (see Section A1) of the badly observed part of the TGAS sky in Fig. B1. Comparing to the overall completeness of the ‘good’ part of the sky in Fig. A4, the completeness in this badly observed part is significantly lower and has artefacts due to the scanning law. The overall completeness of this part of the sky is also shown in Fig. B2 split into the four main reasons why a part of the sky is not included in the ‘good’ part.

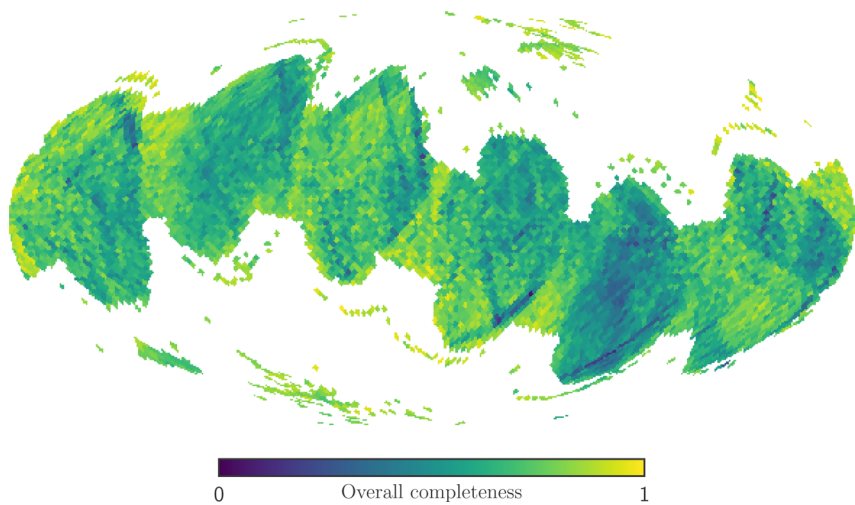


Figure B1. Overall completeness in the ≈ 52 per cent of the sky that fails our TGAS observational quality cuts. Compared to Fig. A4, it is clear that the completeness in this part of the sky is lower and has more artificial structure than in the ‘good’ 48 per cent of the sky.

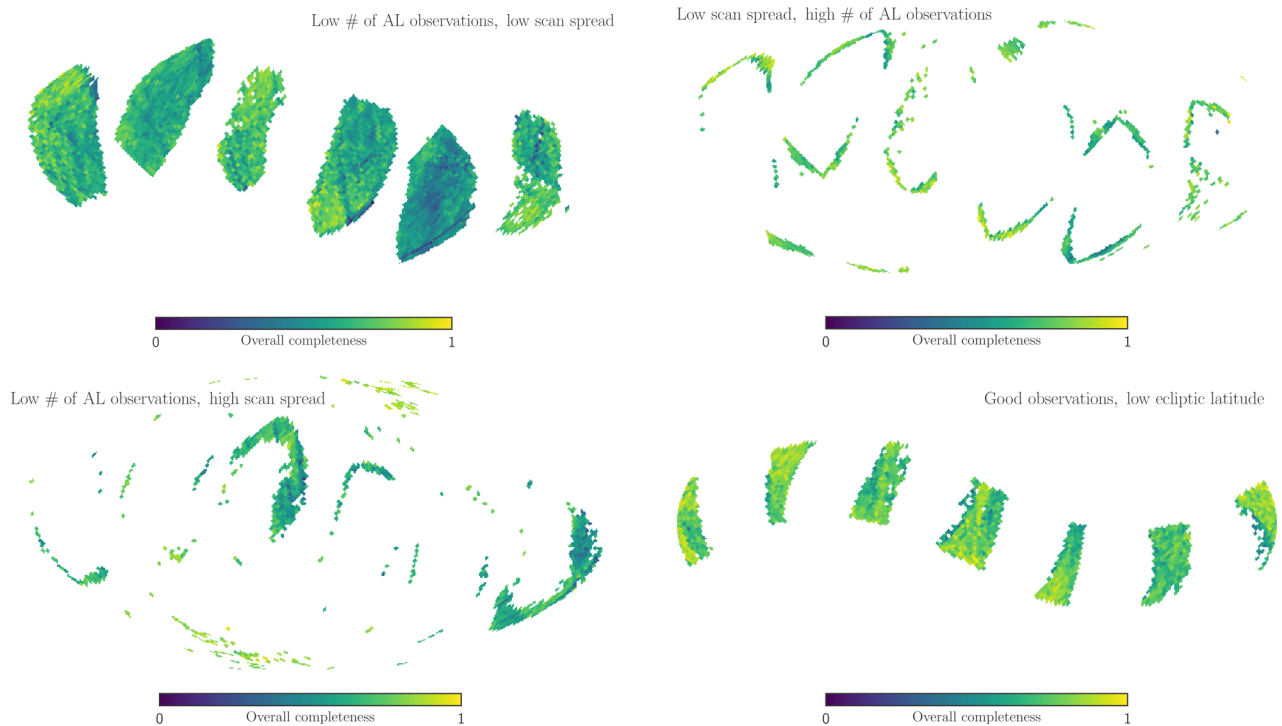


Figure B2. Overall completeness in the ≈ 52 per cent of the sky that fails our TGAS observational quality cuts like in Fig. B1, but split into four categories of reasons why these regions fail our cuts.

This paper has been typeset from a $\text{\TeX}/\text{\LaTeX}$ file prepared by the author.